UNIVERSITY OF CALIFORNIA,
IRVINE

Engineering Scalable Multiplexed Molecular Screening Platforms

DISSERTATION

submitted in partial satisfaction of the requirements
for the degree of

DOCTOR OF PHILOSOPHY

in Biomedical Engineering

by

Hinesh V. Patel

Dissertation Committee:
Associate Professor, Elliot E. Hui, Co-Chair
Associate Professor, Jered B. Haun, Co-Chair
Professor, Abraham P. Lee, BME

2021

DEDICATION

To Emma,

You have been a guiding light in stormy weather,
and enduring partner in all of life's adventure...

TABLE OF CONTENTS

LIST OF FIGURES

ACKNOWLEDGMENTS

There are a host of key figures who have not only enabled me to complete this work but have also been instrumental in my growth over the years as a scientist and an individual.

I'd like to acknowledge both of my advisors, Dr. Elliot Hui and Dr. Jered Haun, for the many opportunities to learn and develop as an independent researcher. In addition, I'd like to thank them for their receptiveness to a non-traditional co-advised arrangement that provided ample room for me to explore and hone a breadth of skills through a combination of scientific endeavors. I'd also like to thank the numerous lab members that served as teachers and friends, making the lab environment both enriching and enjoyable. Additionally, I'd like to acknowledge my thesis committee members Dr. Abraham P. Lee, Dr. Robert Edwards, and Dr. Enrico Gratton for their support, constructive feedback, and scientific guidance.

I would also like to thank the numerous students, faculty, and industry members in The Center for Advanced Design and Manufacturing of Integrated Microfluidics (CADMIM); especially Dr. Sylvia Soehner for continued support, funding, and mentorship on the microfluidic work.

I am incredibly thankful to the UCI Medical Scientist Training Program, Dr. Al Goldin, Dr. Edwin Monuki, and Joanne Wu for fostering a warm community of clinician scientists and medical scientists in training. I feel fortunate and empowered to be among individuals that complement rigorous scientific pursuits with integrity and compassion for those we seek to help; whether clinically or through translational work. In addition, UCI MSTP provided an incredible amount of support in helping me navigate and return to a meaningful career after a significant medical leave.

Personal and programmatic support was funded through the UCI MSTP Program. The microfluidic work was funded through a combination of CADMIM, KWS SAAT SE & Co. KGaA, and the National Science Foundation (NSF) Partnerships for Innovation Award (PFI). The FLIM work was funded through the National Institutes of Health (NIH) R21.

I'd like to express deep gratitude for the range of support from my family; especially my parents and brothers. My mother in particular is to thank for her enduring selflessness and kindness as I figured things out; and even patience and companionship during many inconvenient caffeine runs!

Thank you to the Bindloss Family for the unconditional support over the years. I've really enjoyed our time spent together from mountains to beaches, and look forward to new memories.

Lastly, thank you Emma - for not only reminding me the joy is in the journey, but for continually encouraging me, challenging me to grow, and filling each day with a lifetime's worth of happiness.

CURRICULUM VITAE

Hinesh V. Patel

EDUCATION

Doctor of Medicine — ***expected* 2023**
University of California, Irvine — *Irvine, CA*

Doctor of Philosophy in Biomedical Engineering — **2021**
University of California, Irvine — *Irvine, CA*

Masters of Science in Biomedical Engineering — **2020**
University of California, Irvine — *Irvine, CA*

Master of Philosophy in Bioengineering — **2015**
Imperial College, London — *London, UK*

Bachelor of Science in Bioengineering, Honors — **2011**
University of California, Berkeley — *Berkeley, CA*

FELLOWSHIPS

Whitaker International Fellows and Scholars Program — **2012–2013**
Imperial College — *London, UK*

NIH Minority Health International Research Training Program — **2011**
Stellenbosch University — *Capetown, ZA*

JOURNAL PUBLICATIONS

1. Metcalf, G.A.D., Shibakawa, A., **Patel, H.**, Sita-Lumsden, A., Zivi, A., Rama, N., Bevan, C.L., Ladame, S. *"Amplification-free detection of circulating microRNA biomarkers from body fluids based on fluorogenic oligonucleotide-templated reaction between engineered peptide nucleic acid probes: application to prostate cancer diagnosis."* Anal. Chem. 88, 8091–8098 (2016).

2. **Patel, H.** *"Sensing of circulating microRNAs using high-throughput droplet-based microfluidics: a non-invasive diagnostic tool for cancer."* Imperial College London (2015).

3. McGahan, P. J., **Patel, H.**, Dickinson, E., Leasure, J. Montgomery III, W. *"The effect of biceps adhesions on glenohumeral range of motion: a cadaveric study.* J. shoulder Elb. Surg. 22, 658–665 (2013).

PODIUM PRESENTATIONS

1. **H.V. Patel**. *"Engineering Scalable Multiplexed Molecular Screening Platforms."* Biomedical Engineering Department Seminar Series, University of California, Irvine (Virtual, 2021).

2. **H.V. Patel**, M.K. Rahim, A. Vallmitjana, E. Gratton, J.B. Haun. *"Highly Multiplexed Molecular Profiling Platform Using Fluorescence Lifetime Imaging Microscopy (FLIM)."* Biomedical Engineering Society Annual Meeting (BMES) (Virtual, 2020).

3. **H.V. Patel**, E.E. Hui. *"Microfluidic High-Density Genotyping Platform."* Center for Advanced Design and Manufacturing of Integrated Microfluidics (CADMIM), Industrial Advisory Board Meeting, University of of Illinois at Chicago (2019).

4. **H.V. Patel**, M.K. Rahim, E. Gratton, J.B. Haun. *"Multiplexed Molecular Analysis using Fluorescence Lifetime Imaging Microscopy (FLIM): Towards Future Cancer Diagnostics."* MSTP Annual Student Symposium, University of California, Los Angeles (2019).

5. **H.V. Patel**, E.E. Hui. *"Droplet KASP Array."* Center for Advanced Design and Manufacturing of Integrated Microfluidics (CADMIM), Industrial Advisory Board Meeting, University of of Illinois at Chicago (Virtual, 2018).

6. **H.V. Patel**, M.K. Rahim, E. Gratton, J.B. Haun. *"Multiplexed Molecular Analysis using Fluorescence Lifetime Imaging Microscopy (FLIM): Towards Future Cancer Diagnostics."* 18th Annual UC System-wide Bioengineering Symposium, University of California, Los Angeles (2017).

7. **H.V. Patel**, S. Ladame. *"Fluorogenic Peptide Nucleic Acid (PNA) probes for the minimally invasive and high-throughput profiling of circulating microRNAs"* Annual Whitaker Grantee Enrichment Seminar, Budapest, Hungary (2013).

8. **H.V. Patel**, R. Henrikson., F.B. Myers, P. van Helden, L.P. Lee. *"An Integrated Microfluidic System for Multiplexed Genotype Analysis in a Point-of-Care Setting."* MHIRT 2011 Fall Student Symposium, University of California, Berkeley (2011).

POSTER PRESENTATIONS

1. **H.V. Patel**, E.E. Hui. *"High-Density Genotyping Array."* Poster presented at: Center for Advanced Design and Manufacturing of Integrated Microfluidics (CADMIM), Industrial Advisory Board Meeting, University of Illinois at Chicago (Virtual, 2020) - *2nd Place Poster Award.*

2. **H.V. Patel**, E.E. Hui. *"Combinatorial Droplet Pairing in Microfluidic Networks via Paraffin Microvalves."* Poster presented at: Center for Advanced Design and Manufacturing of Integrated Microfluidics (CADMIM), Industrial Advisory Board Meeting, University of California, Irvine (2020).

3. **H.V. Patel**, E.E. Hui. *"Thermally Actuated Paraffin Microvalves for Dynamically Tuning Membrane Permeability."* Poster presented at: Center for Advanced Design and Manufacturing of Integrated Microfluidics (CADMIM), Industrial Advisory Board Meeting, University of Illinois at Chicago (2019).

4. **H.V. Patel**, E.E. Hui. *"Microfabrication strategies of layered two-phase fluidic circuits."* Poster presented at: Center for Advanced Design and Manufacturing of Integrated Microfluidics (CADMIM), Industrial Advisory Board Meeting, University of California, Irvine (2019).

5. **H.V. Patel**, E.E. Hui. *"Two-Phase Flow Bounded by Porous Walls."* Poster presented at: Center for Advanced Design and Manufacturing of Integrated Microfluidics (CADMIM), Industrial Advisory Board Meeting, University of California, Irvine (2017).

INTELLECTUAL PROPERTY

E.E Hui, H.V. Patel, 2020. ***Microfluidic Phase-Change Membrane Valves***
UCI Case No. 2020-635-1; (Patent Pending)

E.E Hui, H.V. Patel, 2017. ***Combinatorial Droplet Array***
UCI Case No. 2017-585-1; (Record of Invention)

ABSTRACT OF THE DISSERTATION

Engineering Scalable Multiplexed Molecular Screening Platforms

By

Hinesh V. Patel

Doctor of Philosophy in Biomedical Engineering

University of California, Irvine, 2021

Associate Professor, Elliot E. Hui, Co-Chair
Associate Professor, Jered B. Haun, Co-Chair

A central role of biomedical research is capturing and evaluating the rich information from genes, proteins, and/or other small molecules to provide actionable information. With modern advances and understanding, focus has shifted to sensing multiple analytes in parallel. Yet, further improvements in multiplexed tools are needed for improved throughput. Here we present two technologies that expand our toolbox for multiplexed molecular screening.

Current standard in biochemical assay multiplexing follows the well-plate paradigm where microliter volumes are spatially separated and retained in wells, maintaining individual addressability of thousands of simultaneous reactions. Preservation of spatially indexed sample wells enables robotic liquid handlers to construct parallel combinatorial reactions. Droplet microfluidics offer facile means of translating reagents into nano- and picoliter reaction vessels at throughput speeds outpacing robotic liquid handlers. However, continuous droplet production usually requires serial methods of droplet fusion, mixing, and sorting. This loss in spatial indexing limits the ability to match well plates in screening combinations of different reagents or compounds. Demonstrated here is a microfluidic method coupled with phase-change gating technology to generate all pairwise combinations

between two sets of reactants, enabling improved multiplexed screening of assay markers across multiple samples. This architecture can preserve spatial indexing with full on/off control of droplet merging, producing deterministic pairwise combinations of original droplets. Such an approach achieves a sharp 30-fold reduction in reagent consumption and nearly 40-fold reduction in liquid handling, suitable for a wide range of applications from medicine to agriculture.

Understanding the molecular heterogeneity within the tumor microenvironment can help characterize host vs. neoplastic cell types, identify metastatic propensity, guide clinical management, or elucidate novel drug targets. Multiplexed molecular profiling that preserves spatial context traditionally requires either spectral differentiation, high-powered imaging equipment, or cyclic techniques involving serially degradative rounds of sample staining and antigen retrieval. Here we demonstrate an imaging platform, leveraging the phasor approach to fluorescence lifetime imaging microscopy (FLIM) and deep learning, to resolve up to 4 exogenous molecular probes. Resolution is achieved within a single spectral window, adding an orthogonal dimension with which to multiplex optical imaging.

1 Multiplexed Microfluidic Platform for Combinatorial Droplet Pairing: *A High-Density Genetic Screening Tool*

1.1 Introduction

Current standard in biochemical assay multiplexing follows the well-plate paradigm where microliter volumes are spatially separated and retained in wells, maintaining individual addressability of thousands of simultaneous reactions in a compact footprint. Critical to the success of the well plate is preservation of sample manipulation based on position to enable parallel combinatorial reactions. Robotic liquid handlers perform reagent addition and mixing operations directly to individual reactions deterministically based on a standardized, spatially indexed format. Historically, improvements in injection molding capabilities drove the reduction of well volumes and increases in well-densities on the same footprint, enabling greater multiplexing. The most common format consists of a 32x48 matrix of 1536 total independent reaction wells with working volumes ranging between 1-10μL. However, further increases in well-density and volume reduction have slowed, encountering technical hurdles[1]. As a result new, innovative approaches are needed for performing high-throughput, multiplexed screens.

Microfluidics comprise an interdisciplinary field burgeoning in recent decades with the promise of large-scale miniaturization and automation of multiplexed biochemical assays. Micro- and nano-fabrication practices from the semiconductor industry have been directed

toward building such miniaturized fluidic systems, with growth analogous to that of the microprocessors[2]. Advances in understanding and maturation of core capabilities has led to a shift towards translational efforts. In coming years, advances in these systems will likely continue to be the epicenter of disruptive innovation in biotechnology and healthcare[3].

Engineered for precise spatiotemporal control and manipulation of fluid volumes at the micro-scale, devices enable scientists to capitalize on behaviors such as efficient heat-mass transfer, dominance of viscous forces, increase in surface energy effects, and overall faster reaction kinetics. Droplet microfluidics offer facile means of translating reagents into nano- and picoliter reaction vessels at throughput speeds outpacing robotic liquid handlers[4]. These technologies offer significant advantages for reduced reagent consumption and increased reaction density on a compact chip[2,3,5].

Various small molecules can be encapsulated in droplets and the resulting high surface area to volume ratios further increase reaction kinetics. These multi-fold volume reductions enable more rapid, efficient, and cost-effective alternatives to bulk analyses[2,6]. As a result, these platforms offer significant opportunities to reduce cost and dramatically increase throughput of many mainstay laboratory functions, including multiplexing biochemical assays[2].

The two most common continuous droplet generation techniques are T-junctions and flow-focusing. T-junctions introduce aqueous phase orthogonally into a continuous stream of an immiscible carrier phase. Flow-focusing junctions direct both phases into a narrow focused nozzle. Both techniques result in an emulsion of discretized liquid plugs suspended in an immiscible phase. However, challenges in commercial adoption remain, centering on multi-device integration efforts, sample tracking, and analytical readout schemes. Though continuous droplet technologies generate at speeds in the kilohertz range, critical integration of spatial tracking and individual droplet reagent addition strategies moderate increases in throughput.

Moreover, continuous droplet production results in 1-dimensional droplet arrays, usually requiring serial methods of droplet fusion, mixing, sorting and interrogation downstream of production. Two main microfluidic technologies to perform reagent additions are direct injection and pairwise droplet merging. Direct injectors, commonly referred to as pico-injectors, rely on the intersection of two channels to introduce new aqueous content to cross flows of droplet plugs. As droplets near channel intersections, volumes of the same aqueous additions are momentarily injected into each passing droplet. In order to add multiple different reagent additions, multiple pico-injectors are arranged in series for the successive introduction of additional droplet content, limiting their ability to match well plates in screening heterogeneous combinations of different reagents or compounds[7].

Alternatively, two different droplet populations can be combined to produce a combinatorial set of new droplets. When performing pairwise droplet merging under continuous operation, two independent streams of droplet plugs are brought together, merging pairs of droplets sequentially. As a result, they suffer from similar limitations in scalability and throughput for combinatorial screening as pico-injectors. Instead, under static droplet operation, droplets are arranged in an arrayed manner analogous to individual wells in a well plate. This architecture can preserve spatial separation and indexing when merging droplets, producing deterministic pairwise combinations of original droplets[7]. However, control of droplet fusion in static operation not only requires methods to simultaneously generate and align distinct arrays of droplets from bulk sample, but also integration of fluidic control elements such as microvalves, to provide full on/off control of interaction between droplets of differing composition.

Therefore, over recent years significant attention and progress has been made towards the development of suitable microvalves[8–13]. However, despite this focus, many of these valves require expensive and bulky off-chip components or complex cleanroom fabrication

processes in order to operate. These inherent limitations preclude them from being low-cost disposable solutions.

Microvalves can be broadly categorized into either active or passive valves. Many conventional active microvalves use a flexible membrane coupled to an electromechanical or pneumatic actuator. Membrane deflection results in opening or closing of microchannels. However, materials often used for flexible membranes exhibit poor thermal conductivity and non-negligible liquid biomolecule absorption. When performing biochemical assays in small fluid volumes at the micro-scale, minor fluctuations in non-specific biomolecule absorption can be detrimental to effective local concentrations, assay reliability, and reproducibility of results[8–11]. An additional result of membrane-actuator coupling is the requirement of additional costly equipment to operate. This becomes an increasingly non-trivial task as the capabilities, size, and density of the devices scale.

One attractive non-mechanical active valve operates through the use of smart materials such as phase-change materials (PCMs). These materials are cheap and disposable making them well suited for LOC applications. They often operate by thermal actuation where a simple heat source induces a solid-to-liquid phase transition. Phase-change material such as paraffin wax have been used as microvalves by either acting to displace elastomeric membranes or as plugs within microchannels that are displaced by capillary forces or pressure differentials once melted. One benefit of phase change materials is low energy consumption as they inherently persist in latched open or closed states. Plug-type actuation valves have typically been single-use and require lengthy fabrication in order to appropriately incorporate paraffin at specific locations within a microfluidic channel network. While researchers have also demonstrated multiple actuation cycles of paraffin wax microvalves in microfluidic devices, there still remain a number of limitations reducing its tractability as a commercial success[8–11].

Previously demonstrated microfluidic wax microvalve technologies exhibit a few key limitations that pose a significant barrier to commercial success. These disadvantages deal primarily with the requirements for fabrication and basic operation of these devices. Firstly, fabrication either requires cleanroom based micro-fabrication techniques, labor-intensive manual application and sealing of wax within microchannels, or a combination of both. The devices then require a pressure differential, during operation, to displace liquid paraffin from the microchannel and open the valve to allow for subsequent fluid flow. While useful for research purposes, many previously published techniques to address some of the inherent limitations of current wax microvalves do not easily scale with current industrial manufacturing processes. As a result, it currently prohibits achieving higher densities of microvalves, and therefore chip capabilities, without concurrently increasing the complexity of operation. One approach is to use local electric heating elements paired with a microvalve as a means of individually addressing microvalves and interfacing with other electrical connections. In most cases, the number of independent heating elements needed to address each microvalve individually, grows linearly with valve densities. Designing such a chip capable of 1536 independent reactions at densities that compare to operations in well plates, would require a non-trivial number of heating elements and electrical connections, thereby increasing chip complexity and cost. While published demonstrations highlight the robustness of paraffin microvalves, specific approaches to-date would require significant channel complexity, time-consuming fabrication, and unrealistic number of pressure or heat inputs in order to operate as true Lab-On-A-Chip technologies[8–11].

Therefore in order for a platform to realize the benefits of microfluidics - volume reduction, increased throughput, and resulting cost savings - new fluidic architecture and microvalves are needed. Demonstrated here is a static droplet microfluidic method coupled with phase-change gating technology to generate all pairwise combinations between two sets of reactants. Self-digitizing droplet arrays, defined on separate layers, control routing, generation, and trapping of aqeuous droplets in specific organized locations. Fluidic

channels on different layers are sealed and partitioned by thin paraffin membranes which serve to provide zero-leakage microvalves between two or more fluid compartments in the microfluidic device. This architecture preserves spatial indexing with full on/off control of droplet merging, producing deterministic pairwise combinations of original droplets. Such an approach achieves a sharp 30-fold reduction in reagent consumption and nearly 40-fold reduction in liquid handling, enabling low-cost, multiplexed screening of assay markers across multiple samples.

1.2 Microfluidic Combinatorial Droplet Pairing

In order to leverage the significant cost and throughput advantages realized by miniaturization, we first developed a scalable strategy for combinatorial droplet pairing. Demonstrated here is a microfluidic method to generate all pairwise combinations between two sets of reactants, enabling improved multiplexed screening of assay markers across multiple samples. The approach discretizes M different samples into an array of M columns of N individual droplets, and N reagents into an array of N rows of M droplets. The result is an MxN matrix where each column corresponds to different sample and each row corresponds to a different assay.

Reactants are discretized into droplets using a previously reported self-digitizing approach that leverages predefined channel geometries to spatially separate and immobilize droplets. Briefly, a droplet well consists of a circular droplet trapping region followed by a channel constriction that acts as a capillary valve. Liquid is driven from a reservoir into a linear channel containing a set of droplet wells connected in series. The capillary valve allows filling but not emptying of the droplet trapping regions. The aqueous liquid is followed by an immiscible phase (oil or air) that displaces aqueous phase from the main channel. The surface tension between the two immiscible phases results in shearing of

aqueous segments that remain behind in droplet wells, controlling both droplet production and spatial indexing[14–17]. As a result, a single μL-volume liquid sample reservoir is discretized into a series of nL-volume droplets with a single fluid stream. Arranging multiple self-digitizing channels in parallel produces a 2-dimensional self-digitizing array.

Samples are distributed across M columns of the array on one layer and reagents are distributed across N rows of the array on a second layer. This becomes useful, for example, in the binary array in **Fig. 1.1**, showing a set of 5 samples (1-5) and a set of 5 reagents (A-E). Each sample must be combined with each reagent individually, creating 25 individual reactions. Droplets from each sample are distributed vertically downwards, **Fig. 1.1A**, while droplets from each reagent are distributed horizontally to the right, **Fig. 1.1B**. Here, the horizontal and vertical paths do cross-contaminate as they are placed on separate fluidic layers. The droplets remain trapped in their respective locations shown. The two independent arrays are orthogonally aligned, situating sample droplets on top of reagent droplets, generating all pairwise combinations of MxN ordered droplet pairs while maintaining their spatial indexing.

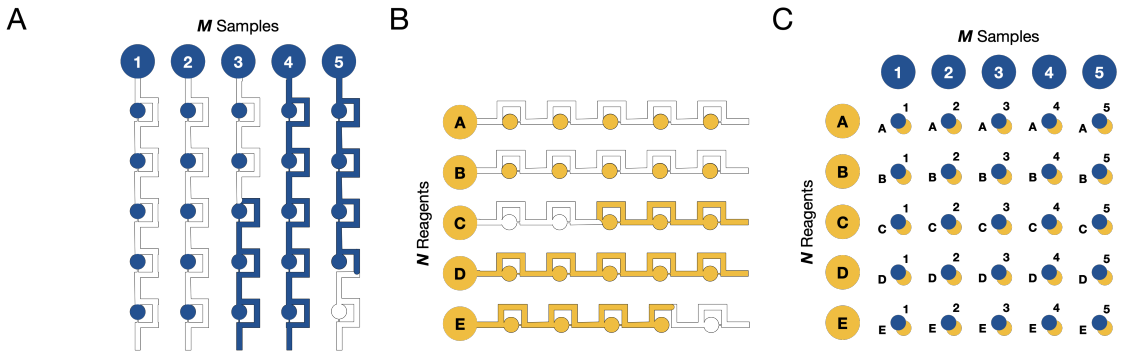

Figure 1.1: Schematic of Combinatorial Droplet Pairing Method. Self-digitizing channels generate arrays of droplets on separate layers. (A) Digitization of 5 different samples into 5 columns of droplets. (B) Digitization of 5 different reagents into 5 rows of droplets. (C) Overlap results in production of all possible combinatorial pairs.

1.3 Phase-Change Membrane Microvalves

In order to demonstrate simultaneous pairwise droplet merging of all MxN ordered droplet pairs, each layer of arrayed droplets is separated by a switchable barrier, providing precise temporal control over sample-reagent fusion. The barrier will be kept in-place during droplet generation on the two independent layers and subsequently removed to drive mixing of contents between all generated droplet pairs simultaneously.

Microvalves, a common switchable barrier, regulate flow between two different fluid filled chambers. Moreover, integration of microvalves is reported as critical for successful miniaturization and commercialization of microfluidic technologies[12,13,18]. However, current microvalve technologies, including those electromechanically or pneumatically driven, either require specialized cleanroom fabrication or difficult multi-layer assembly. Additionally, these valves exhibit drift in valve integrity or require multiple input lines for robust actuation of valves in parallel. Row-column addressing schemes can greatly reduce the number of required input lines, yet still scale linearly with each additional column or row of valves. As a result, manufacturing and operating such valves between every ordered droplet pair would prove too costly, limiting affordable scalability.

1.3.1 Dynamically Tunable Membrane Valves

Due to a lack of suitable microvalves, we derived a new microvalve technology from phase-change materials (PCM). Paraffin wax, a widely available and inert phase-change material, has previously been used in molecular biology. Commonly used to maintain separation of PCR reagents at room temperature, the solid paraffin prevents off-target and non-specific byproducts prior to thermocycling and amplification. Inspired from this approach, we sought to miniaturize this method by fabricating and incorporating thin,

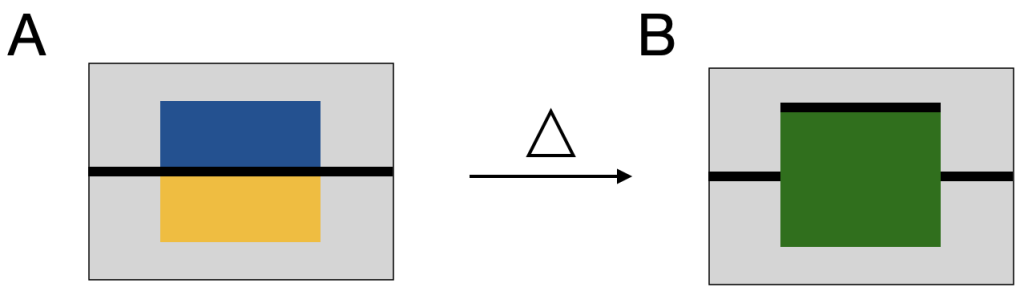

Figure 1.2: Schematic of Phase-Change Thermal Valve. (A) A thin layer of solid phase-change material separating two different fluid compartments. (B) The introduction of energy (heat) induces a phase-change from solid to liquid resulting in mixing of the two previously separated fluid compartments.

membrane-like sheets of paraffin to separate two or more overlapping microfluidic chambers. At room temperature, paraffin is solid, blocking fluid from traveling between the first and second microfluidic layers, **Fig.1.2A**. Application of heat to the entirety of the device drives the transition of the paraffin from a solid to a liquid. The entire liquefied membrane is displaced from regions between two overlapping chambers, resulting in mixing of the contents of the two previously separated chambers **Fig.1.2B**. As a result, the thin paraffin membrane acts as a low-cost thermally actuated microvalve.

To demonstrate fluidic sealing of thin paraffin membranes between two fluidic layers, we adapted paraffin tissue sectioning techniques that are a mainstay of histological specimen preparation. First, microfluidic devices were fabricated using previously reported techniques. A silicon master mold was created using a custom dry-resist photolithography setup and commercially printed photomasks patterned with 5x5 self-digitizing arrays. Droplet traps were designed with a pitch of 2.25mm, analogous to well spacing in a standard 1536 microtiter plate. Then polydimethylsiloxane (PDMS) elastomeric devices were produced by standard soft-lithography. Briefly, a 10:1 ratio-metric mixture of pre-polymer to curing agent were mixed and cast on to the silicon master. After polymer curing, final devices were peeled and cut to correct dimensions (approx. 25x25mm). Second, with a sliding microtome, micron-thick membranes are sectioned from a block of

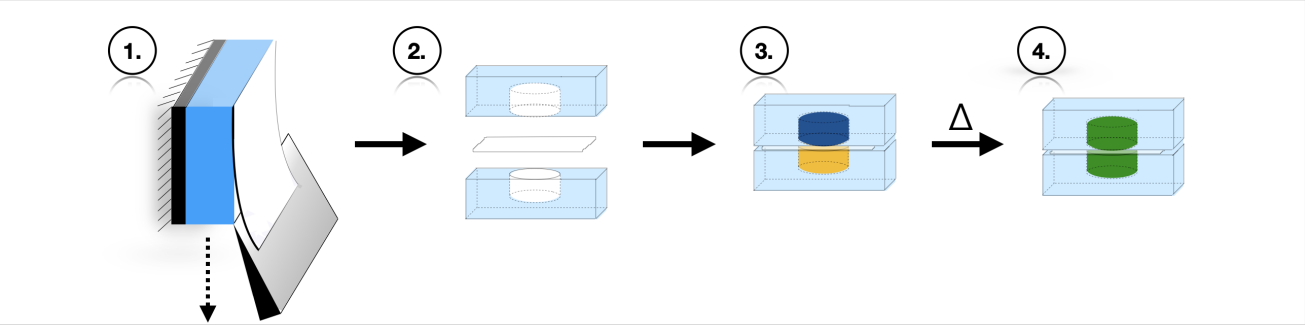

Figure 1.3: Schematic of Membrane Microvalve Fabrication and Assembly.

pure paraffin wax and sandwiched between two PDMS microfluidic devices as depicted by the schematic in **Fig.1.3**. The face with exposed channels are sealed with paraffin membranes analogously to mounting tissue sections on glass slides in preparation for immunohistochemistry. Newly sectioned paraffin membranes are place in a 42°C heated water bath, softening and restoring planarity of the membrane, **Fig.1.4A**. Unsealed microfluidic devices are submerged in the water bath and directed toward the membrane from below. Once in contact, water is displaced from between the device and membrane, resulting in the softened paraffin uniformly adhering, **Fig.1.4B**.

Since paraffin is solid at room temperature, the membrane serves as a floor or ceiling of each droplet array, providing the necessary fluidic seal for independent droplet production while preventing cross-contamination. We first demonstrated the strength of

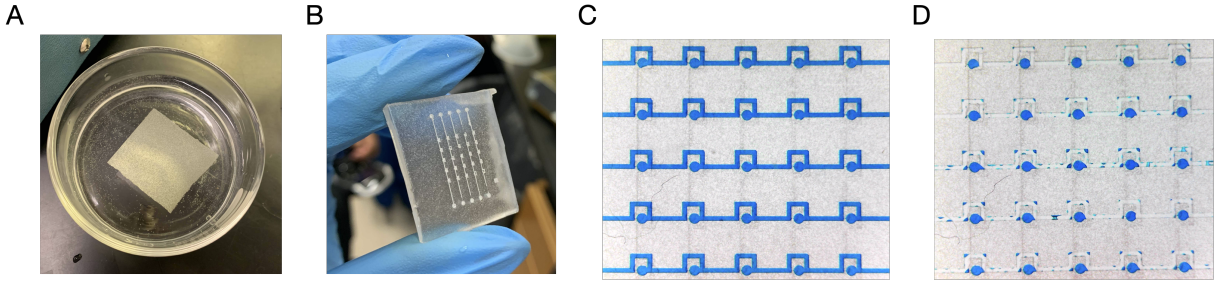

Figure 1.4: Fluidic Handling of Membrane Microvalves. (A) Planarity restored to newly sectioned paraffin. (B) Sealing of a PDMS device, containing a 5x5 self-digitizing array, with a paraffin membrane. (C) Initial loading of aqueous blue dye in each channel, filling droplet traps. (C) Displacement of aqueous blue dye from main channels using air, resulting in digitization of a 5x5 droplet array.

seal and fluid handling in a single-layer sealed device. Aqueous blue dye was loaded into each row of a 5x5 droplet array, completely filling the self-digitizing channels and droplet traps. The quality of liquid seal afforded by the paraffin membrane is made visually apparent by the colored dye. Dye is completely confined to within the channel walls and droplet traps, shown in **Fig.1.4C**. Next, a plug of air, dispensed into each channel, evacuated the dye. As a result of the self-digitizing approach, a series of droplets containing blue dye remained pinned behind in static locations specified by the predefined channel geometry. A 2.25mm pitch resulted in droplet reaction chambers spaced equally to the wells of a 1536-well microtiter plate, yet witth a fraction of the required volume. Evident containment of liquid within the microchannels, without leakage of fluid in between rows of the device, further highlights the quality of fluidic sealing,**Fig.1.4D**. However, a number of regions, particularly corners, of a single channel contain remnants of dye. The effect is a result of the interaction between dye wetting the channel walls and sharp corners providing regions of increased wettability. A combination of rounded channels and surface treatment of channel walls with readily available reagents to increase hydrophobicity, would eliminate the effect.

1.3.2 Single Membrane Valved Droplet Array

Next, a layered device with two droplet arrays orthogonally aligned across a single membrane layer demonstrates both independent fluidic operation and simultaneous pairwise droplet merging. An empty 5x5 PDMS droplet array was sealed with a 70μm thick sectioned paraffin membrane. A second empty 5x5 PDMS droplet array was orthogonally aligned, overlapping droplet trapping regions, and mechanically fixed in position to prevent loss of alignment during operation. First, a blue aqueous dye was introduced and digitized across all rows of the top fluidic layer, leaving behind an array of static blue droplets **Fig.1.5A**. Then, yellow dye was introduced across all columns of the

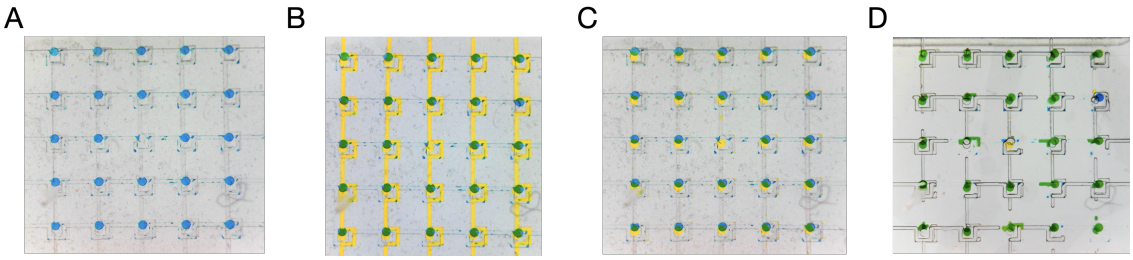

Figure 1.5: Single Membrane Layer Combinatorial Droplet Array. (A) Aqueous blue droplets digitized across rows of a 5x5 self-digitizing array top layer. (B) Yellow aqueous dye independently filling columns of a 5x5 self-digitizing array bottom layer. (C) Following digitization of yellow droplets produces combinatorial blue-yellow droplet pairs across a single paraffin membrane layer. (D) Pairwise droplet mixing following thermal microvalve actuation.

bottom fluidic layer and digitized leaving behind an array of yellow droplets. The result positioned yellow droplets underneath the blue droplets, separated by the paraffin membrane, **Fig.1.5B,C**. All but 2 of the 25 possible droplet pairs were generated, likely due to preexisting device defects during fabrication that resulted in corrupted capillary valves. Blue and yellow colored dyes were chosen to produce a green color upon mixing, making rapid visualization of leaks apparent. Interestingly, blue-yellow droplet pairs remain distinct in color and spatially ordered, demonstrating combinatorial pairing of microfluidic droplets. Additionally, the absence of visible green color in arrayed droplets at room temperature, **Fig.1.5C**, suggests no mixing has yet occurred. Since paraffin is solid at room temperature, the membrane exists in an initially "latched closed" position, acting as a zero-leakage valve that enables droplet generation on each layer independently.

To demonstrate valve actuation and controlled droplet fusion, the device was placed in a heated oven for 15 minutes at 95°C, a temperature well over paraffin melting temperature of 56°C. Application of heat melts the entire paraffin layer which seemingly leaves the structure vulnerable to leaking. However, green color, indicative of droplet mixing, is present across all 23 regions where droplet pairs had previously been generated, suggesting 100% mixing efficiency when alignment and channel integrity is optimal, **Fig.1.5D** Interestingly, spatial indexing of order droplet pairs is maintained despite membrane

melting. The data suggests dominance of surface tension forces at the microscale become advantageous here. Regions outside the overlapping droplet traps remain immobilized in part as a result of surface tension between the channel walls and the liquid paraffin and no direct leaking occurs. At the same time, once the thin paraffin layer melts it becomes unstable in regions where paraffin is suspended between two fluid-filled channels or chambers. In these overlapping regions, the buoyancy of melted paraffin and the surface tension between liquid paraffin and channel walls drive valve opening. During this process the melted paraffin expands producing an instability that displaces the paraffin to the ceiling of the upper channel layer, allowing a connection to be formed between the previously separated droplets. The result is a "latched open" valve configuration and mixing of the two fluids.

1.3.3 Double Membrane Valved Droplet Array

Although the use of a single paraffin membrane between self-digitizing layers is sufficient to generate droplets on the two independent layers, only one layer is uniformly sealed with paraffin prior to assembly. The second layer is pressure sealed during assembly by mechanical clamping. This results in a greater variability of seal integrity, dependent on

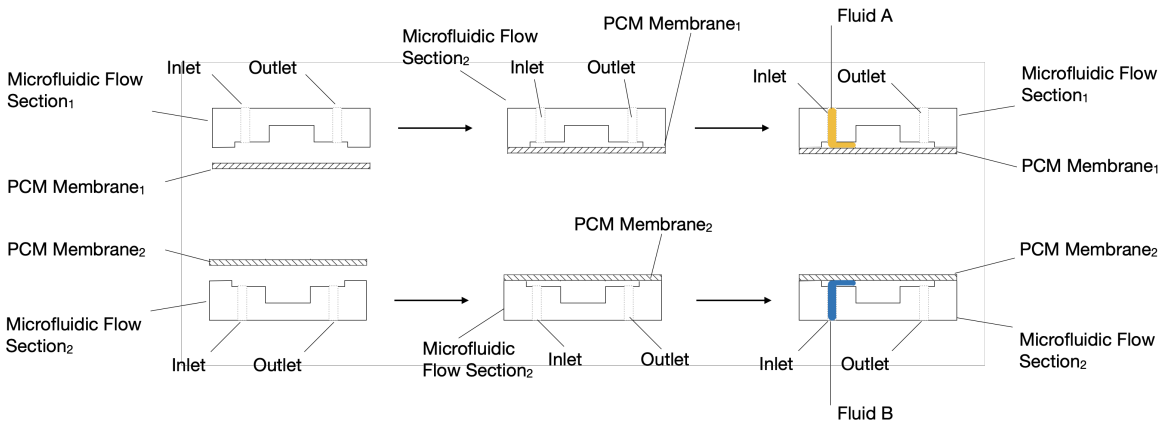

Figure 1.6: Schematic of Double Membrane Layer Assembly & Loading. Independent sealing of each device layer allows separate fluidic operation and assembly.

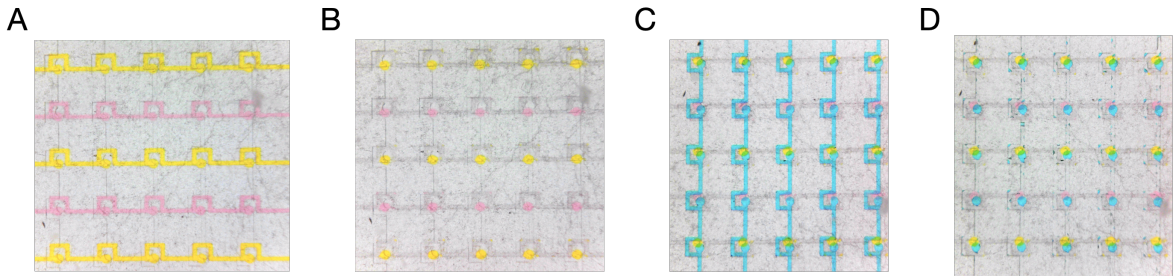

Figure 1.7: Double Membrane Layer Combinatorial Droplet Array.(A) Alternating rows of yellow and red aqueous dye across rows of a 5x5 self-digitizing array bottom layer demonstrating multiplexed testing of different reactants. (B) Fully digitized, heterogeneous population of yellow and red aqueous droplets in a 5x5 self-digitizing array bottom layer. (C) Filling columns of a 5x5 self-digitizing array top layer with aqueous blue dye. (D) Following digitization of blue droplets produces a mixed pairwise combinatorial population of either blue-yellow or blue-red droplet pairs across a double paraffin membrane layer.

clamping mechanism and even distribution of force. A clamp seal increases the opportunity for particulate to become trapped between the channel surface and the membrane, facilitating routes of channel leaking during filling if a uniform seal was not achieved. While the paraffin membrane still maintains separation of the two independent fluid layers, sealing of parallel microchannels within a single layer remains compromised. Leaking between two parallel channels negatively affects the balance of hydrodynamic resistances within a single channel, otherwise necessary for droplet digitization, leading to reduced efficacy of droplet generation. To prevent compromise of channel integrity, each layer was sealed with independent paraffin membranes prior to assembly instead, schematically depicted in **Fig.1.6**.

Two 5x5 droplet arrays were each sealed with a paraffin membrane and each resulting layer functioned as a complete single layer microfluidic device. The rows of one layer were filled with alternating yellow and red dye followed by an air plug to evacuate channels and generate a mixed population of droplets,**Fig.1.7A,B**. Columns of a second layer were filled with blue dye and digitized separately, **Fig.1.7C**. Layers were orthogonality aligned, positioning droplets on top of one another, generating all 25 pairwise combinations between blue droplets and alternating yellow and red droplets, **Fig.1.7D**. The data suggests

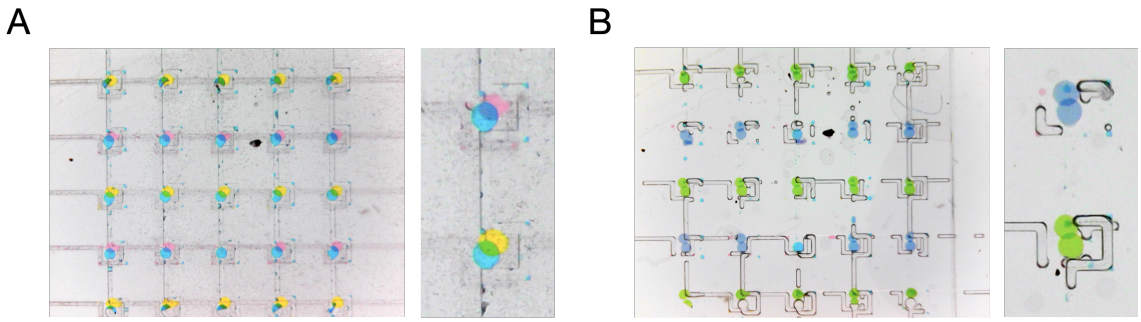

Figure 1.8: Double Membrane Layer Combinatorial Droplet Merging. (A) Left, 5x5 combinatorial droplet array with a mixed population of droplet pairs. Right, close-up of a single blue-red and blue-yellow droplet pair separated by a double paraffin membrane prior to merging. (B) 5x5 combinatorial droplet array with a mixed population of merged droplet pairs. Right, close-up of a merged blue-red and merged blue-yellow droplet pair, resulting in production of droplets with a purple-blue and green color respectively.

sealing, operating, storing, and handling of each layer separately, prior to assembly and microvalve actuation, leads to more flexible and robust fluidic handling and operation. Additionally, loading each row of the bottom layer with contents of differing composition (yellow or red dye), conceptually demonstrates multiplexed testing of different assays across 5 samples for 25 total independent reactions. Furthermore, it becomes readily conceivable that both assay and sample multiplexing can be scaled by incorporating additional channels and assigning different contents to each row and column respectively.

Finally, to demonstrate droplet fusion in a two membrane layered device, the device was placed in a heated oven for 15 minutes at 95°C to melt both paraffin layers. In this experiment green color is produced as a result of blue and yellow droplet fusion and a darker purple-blue is produced as a result of red and blue droplet fusion. The result is alternating rows of green and purple-blue indicating successful droplet merging, shown in **Fig.1.8**. In this experiment 100% of generated droplet pairs merged, producing an indicative color change. Interestingly, the additional thickness of the membrane layer did not impede merging and maintained spatial indexing, pinning each reaction chamber in place. For both single and double membrane layer experiments, an operating temperature of 95°C was chosen because hot-start activation of PCR polymerases occur at the same

temperature. As a result, both valve operation and hot-start can be achieved at a single temperature, indicating device applicability as a multiplexed genetic screening platform. In such a platform, droplet rows may consist of target DNA samples and droplet columns may consist of primer sets against differing sequences of interest.

1.3.4 Commercialization Potential

Integration of the microfluidic self-digitizing approach significantly reduces operation complexity compared to multiplexing in standard well plates. Loading and subsequent reagent additions in traditional MxN well-plate are performed sequentially, resulting in 2xMxN pipetting steps necessary to construct all possible combinations between M+N reactants. For a standard 1536 well plate, generating all combinations between 32x48 samples and reagents requires 3,072 pipetting operations for a single plate. Although mostly automated, this results in longer turnaround times, additional consumable costs, and a larger demand on mechanical equipment subject to wear and costly repair. In contrast, the self-digitization method described requires only M+N pipetting operations for initial liquid reservoir loading. Lastly, both aqueous and continuous phases are capable of being driven under either positive or negative pressure. This suggests liquid reservoir loading and droplet generation require minimal alteration for integration with current robotic liquid handlers. This compatibility may reduce barriers to adoption by further amplifying throughput without requiring workflow overhaul or expensive external commercial systems for microfluidic chip operation.

For the same 1536 well plate setup, the described method requires only 80 pipetting steps to construct all combinations of 32 reagents and 48 samples. Moreover, the principle scales with any size and multiple of MxN rows and columns, **Fig. 1.9A**. Additionally, a comparison of the cost per data point was made for current commercial technologies

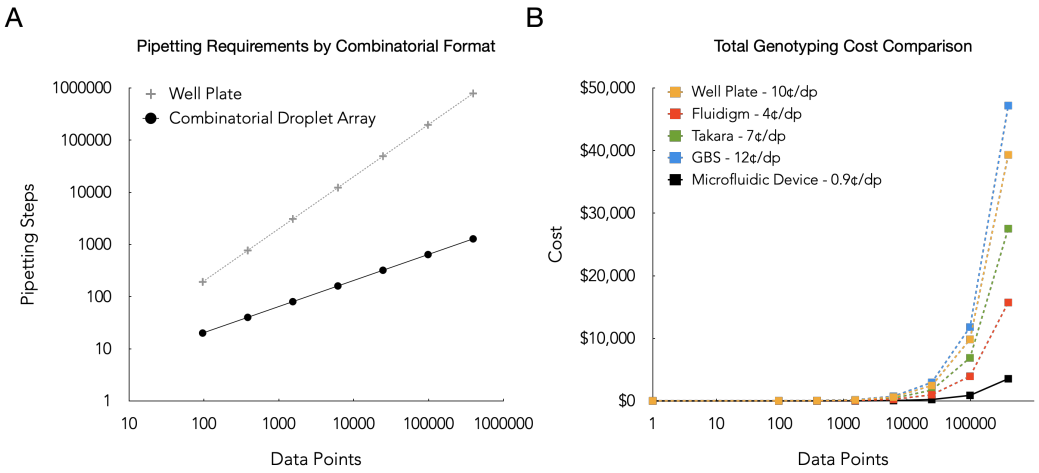

Figure 1.9: Operational and Cost Advantages of Microfluidic Droplet Array. (A) Comparison of pipetting steps by desired data points between well plates and a microfluidic droplet platform. Pipetting steps calculated based on a matrix organization of desired data points. (B) Comparison of cost associated with increasing number of data points across related technologies and a microfluidic droplet platform. Projections based on determined cost/dp.

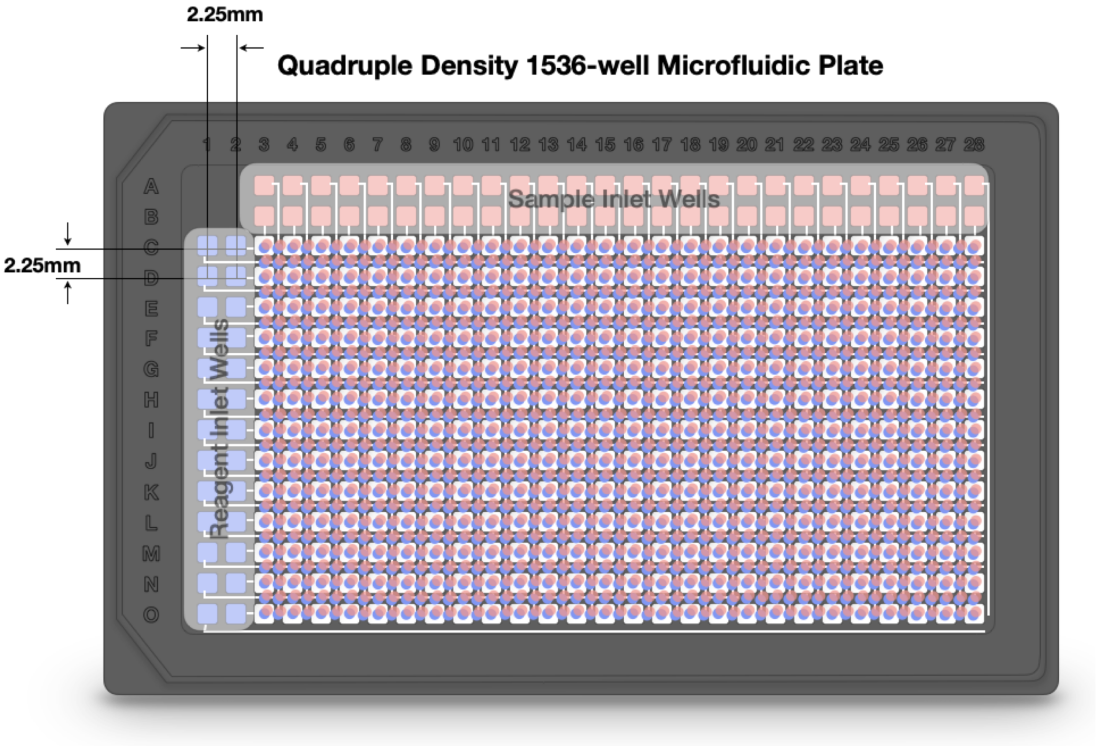

Figure 1.10: Diagram of Commercial Microfluidic Device.

available to multiplex a widely use genotyping assay, **Fig. 1.9B**[19]. This suggests the combinatorial droplet pairing method described is both cost-effective and commercially scalable for use in multiplexing biochemical assays. Leveraging the volume reduction benefits of miniaturization also enables packing droplet wells at a greater density per plate compared to that of a 1536 well plate. As a final component of this work, we designed a microfluidic plate with 4x well density that achieves up to 30-fold reduction in reaction volume and more than 70-fold reduction in necessary pipetting operations, reducing costs associated with both reagent and consumable consumption, **Fig. 1.10**.

1.4 Conclusion

Lab-on-a-Chip technologies seek to consolidate routine laboratory functions into compact and paralellizable microfluidic circuits with integrated control elements, increasing operational throughput while significantly reducing cost. Current standard in biochemical assay multiplexing follows the well-plate paradigm where microliter volumes are spatially separated and retained in wells maintaining individual addressability of thousands of simultaneous reactions. Preservation of spatially indexed sample wells enables robotic liquid handlers to construct parallel combinatorial reactions. However, commercial development and discovery demands outpace the throughput and affordability well plates offer.

Droplet microfluidics offer facile means of translating reagents into nano- and picoliter reaction vessels at throughput speeds outpacing robotic liquid handlers. However, continuous droplet production usually requires serial methods of droplet manipulation, limiting spatially indexed screening of combinations of different reagents or compounds. Moreover, microvalves are another important component of truly integrated microfluidics and significant progress has been made in developing suitable microvalves based on a

variety of actuation mechanisms including electric, magnetic, pneumatic, material-based, acoustic, and more. Despite this abundance, challenges such as leakage, reliability, complexity and cost remain. Demonstrated here is a static droplet microfluidic method coupled with phase-change gating technology to generate all pair-wise combinations between two sets of reactants, enabling improved multiplexed screening of assay markers across multiple samples. Two 5x5 self-digitizing droplet arrays are defined on separate layers for the purpose of routing, generating and trapping aqueous droplets in specific organized locations in preparation for merging. Fluidic channels on different layers are sealed and partitioned by thin paraffin membranes which serve to provide zero-leakage microvalves between two or more fluid compartments in a microfluidic device. Importantly, paraffin membrane microvalves enable droplet generation on the two independent microfluidic layers, allowing arrays of droplets on different layers to overlap one another without interfering with each other. Additionally, the entire paraffin membrane functions to valve all arrayed droplet pairs simultaneously, requiring only a single heat input to remove the membrane barrier and control droplet merging.

This architecture can preserve spatial indexing with low cost and full on/off control of droplet merging, producing all pairwise combinations of original droplets. Such an approach achieves a sharp 30-fold reduction reagent consumption and nearly 40-fold reduction in liquid handling, providing cost-advantage and throughput suitable for a wide range of applications from medicine to agriculture.

1.5 Future Perspectives: A Forward Look

As global population grows, food production struggles to keep pace. By 2050 the world's population is estimated to increase by 35%. To meet this growing food demand, crop production must increase by 200%. With a reduction in arable land, efficiency of crop

production becomes critical. Plant genotyping is used to selectively breed crops with desirable traits. Genotyping is performed by Kompetitive Allele Specific PCR (KASP) to detect single nucleotide polymorphisms (SNPs) and one reaction between a primer set and sample detects one SNP. Currently, hundreds of thousands of reactions are performed daily, up to billions per year, with an expected 25% growth each year. We anticipate the advances in microfluidic combinatorial droplet pairing and new paraffin microvalve technology can be used to develop a scalable, low-cost, and high-throughput genotyping platform to meet industry needs.

Additional future avenues include an adaptable platform for community surveillance of infectious pathogens. PCR-based methods are the gold standard for detection of infectious agents. At low prevalence, pooling strategies are employed where the likelihood of negative results allows combined testing of multiple samples to reduce cost and time. Positive results then necessitate further testing to identify the source sample. Not only is the molecular environment noisier in batched samples, multiplexed testing requires significant validation of primer sets to prevent off-target effects, including primer dimers and non-specific amplification. The balance of high-throughput with spatial indexing afforded by the work described here, offers significant potential for use in multiplexed screening. Since reactions are spatially separated, primer interactions are avoided, simplifying new primer design and validation. As a result, disease specific primers can be optimized more rapidly and mass testing deployed more readily, the need for which has been made evident by the recent Sars-CoV-2 global pandemic.

2 Multiplexed Phasor Fluorescence Lifetime Imaging Microscopy (Phasor FLIM) and Deep Learning: *Building a High-Content Molecular Profiling Tool*

2.1 Introduction

Over recent years, there has been a shift in characterizing tumors beyond the reductionist view as a homogeneous neoplastic mass to a rather rich and heterogeneous one[20]. As a result, cancer's complexity is better understood from the context of the molecular and cellular heterogeneity inherent to the tumor microenvironment.

The practice of molecular sub-typing, or categorization of tissues based on shared characteristics is routine in clinical management of breast cancer. Sub-typing molecular expression of the estrogen receptor (ER), progesterone receptor (PR), and human epidermal growth factor receptor (HER-2) serve to determine candidate therapeutic approaches. Over-expression of ER/PR is associated with response to anti-estrogenic agents while over-amplification of HER-2 is associated with response to targeted immunotherapies. However, instances of tumors negative for all three (triple negative breast cancer, TNBC) lack targeted therapies resulting in an overall poorer prognosis that may benefit from more aggressive treatment. Thus, understanding the dynamics of molecular level expression becomes increasingly important to the development of robust diagnostic tools and selection of pertinent interventions for a leading cause of death worldwide[20,21].

In addition to molecular sub-typing, categorization of the diversity of cell types and functional states within pathological tissue reveals the complex interactions of disease progression. These interactions are characterized by deregulated signaling, inflammation, and various histopathological changes. The tumor microenvironment is a heterogeneous mixture of various host and neoplastic cell types. Host cell types include lymphocytes and their progenitors, granulocytes, tumor infiltrating macrophages (M1 or M2 spectrum), endothelial cells, and more. Neoplastic cell types exhibit a gradient of capabilities from immunosurveillance to distant tumor initiation, derived from epithelial-to-mesenchymal transitions or other similar metastatic induction programs[20,22–25]. Discerning the presence and characteristics of tumor-infiltrating lymphocytes (TILs) in particular, have been correlated with better outcomes for breast, colorectal, and other cancers[26–30]. For example, tumors exhibiting high lymphocytic infiltrate, as assessed via the Immunoscore panel (CD3+, CD8+, CD45RO+), are reported to have longer disease-free survival after primary tumor resection[31–34]. In addition, higher levels of TILs are indicative of stronger chemotherapeutic responses and better overall survival, particularly in triple negative and HER2+ breast cancer[35]. However, these previous studies have relied on capturing the extent of lymphocytic infiltration using standard hemotoxylin and eosin (H&E) and immunohistochemical (IHC) staining of tumor sections. Given the known complexity of lymphocyte subpopulations, higher granularity of molecular characterization of TILs may add greater specificity and sensitivity towards the development of improved diagnostic platforms[36].

As a result, a large focus is placed on improving high-content methods for molecular profiling to capture and contextualize the rich molecular and cellular heterogeneity within the tumor microenvironment. Among numerous high-dimensional techniques, genomic profiling technologies such as DNA microarrays and next-generation sequencing provide a wealth of information. However, many of these -omics techniques are often sample destructive and overlook the spatial context otherwise captured in microscopy-based

methods. Optical imaging enables the study of cells within their native spatial context, detailing morphological and categorical features. Paired with specific molecular interrogation, optical imaging reveals key markers characteristic of cell identity, functional state, intercellular, and environmental interactions. This comprehensive analysis can be used to identify unique functional drivers, as well as distinct cellular niches that likely influence normal tissue function and abnormal disease states[37–40]. Furthermore, in the context of disease, these cellular expression profiles and interactions can provide diagnostic value and insight into disease progression, elucidating potential avenues for targeted therapies[41–44].

Conventional immunofluorescence is a common optical imaging technique that captures both morphology and molecular information. However, a more representative analysis of heterogenous tissues requires a higher degree of multiplexing that surpasses the capacity of traditional fluorescence microscopy; typically limited by spectral overlap to 3-5 markers[45]. The use of narrow emission band quantum dots and hyperspectral strategies afford only modest gains in multiplicity[46–48]. To some extent, cyclic staining methods address the multiplexing barrier with iterative rounds of spectral fluorescence, enabling detection of as many as 40 targets[49–51]. However, cyclic approaches are time-consuming, limited to fixed or frozen samples, and too risk potential sample degradation with each round of processing. Mass spectrometry-based techniques rely on heavy metal reporters, instead of fluorophores, to extend multiplexing capabilities to assess over 40 targets; but these require expensive specialized instrumentation and lengthy time-scales for sub-micron resolution[52]. Ultimately, there is a lack of adequate, scalable, and integrable tools that profile tumor tissue and provide apposite spatial mapping of the molecular and cellular heterogeneity necessary to more intelligently guide clinical cancer management. Extending the spatially informative and quantitative advantages of immunofluorescence at higher throughputs would address current limitations and provide actionable clinical insight[53,54]. To achieve broad adaptability, an ideal multiplexed imaging technique would not only

preserve sample integrity over time, but also be fast, scalable, and compatible with current infrastructure.

Fluorescence lifetime is a measure of the duration of fluorescence emission decay following an excitation pulse; a fundamental property of fluorescent species. Thus, lifetime provides an alternative property, beyond spectral emission, to distinguish multiple fluorescent probes within the same spectral window. Fluorescence lifetime imaging microscopy (FLIM) involves the pixel-by-pixel measurement of lifetime decay within an image and requires only a simple, inexpensive addition to conventional laser scanning microscopes[55]. Previous attempts to resolve fluorescent probes based on lifetime relied on complex fitting strategies, where there are often insufficient photons from experimental data to accurately distinguish between similar lifetimes[56]. Alternatively, pattern-matching techniques that rely on both lifetime and spectral information to more accurately resolve fluorescent probes, still lack sufficient power to unmix combinations of several probes within a single pixel[57].

The phasor approach to FLIM transforms fluorescence intensity and harmonic lifetime signals from each pixel of an image into a geometric-graphical representation of lifetime decay data following previously reported methods[58]. Briefly, phase-delay and modulation ratios, determined by differences between repetitive intensity modulated excitation light and sample derived fluorescence emission, undergo sine and cosine Fourier transforms to graphically map polar coordinates onto the unit circle. As a result of the mapping, mono-exponential decays appear on the unit circle and increasingly complex multi-exponential decays appear further within the unit circle. Shorter lifetimes appear nearer [1,0] and longer lifetimes, represented by a larger phase angle, appear nearer the origin. A nonlinear spectrum of lifetimes fall in between, following the arc of the unit circle. By the nature of the transformation, coordinates in phasor space obey a law of

linear combination. Lifetimes of each pixel in an image are a vectorial summation of relative fractional contributions of the lifetimes of each pure fluorescent species present.

To-date, much work has been done to resolve combinations of endogenous fluorescent molecules for fit-free characterization of cellular metabolic state[59]. With the product of signal intensity and fractional lifetime, this approach can be extended to resolve mixtures of exogenous molecular probes (FLIM-probes) in cellular environments, enabling multiplexed molecular detection. As a result, a single recorded image, stained with multiple FLIM-probes simultaneously, can be deconstructed into individual immunofluorescence images derived from each particular FLIM-probe. In this way, original total intensity of FLIM-probe stained images become analogous to multi-channel composite images, without the need for serial capture or spectrally separate probes. In order to unmix total intensity images into their resulting channels, lifetime fractions for each channel are first determined on a pixel by pixel basis. A system of equations describes the linear combination of pure species lifetimes to each pixel, and the analytical solution quantifies the fractional lifetime contribution of each channel,[60]. This enables algorithmic, quantitative, and fit-free unmixing of multiple fluorescent probes within the same spectral window, using lifetime information alone. An approach otherwise difficult to achieve using standard immunofluorescence techniques and filters.

Importantly, linear orthogonality of FLIM-probe phasor locations is critical to ensuring linear independence and a non-trivial unique solution to the system of equations. However, currently limited availability of intensity-matched, spectrally-matched long-lifetime fluorescent probes makes selection of multiple unique, linearly independent FLIM-probes a non-trivial task. This work first demonstrates multiplexing of 3 FLIM-probes targeting spatially distinct cellular targets. Next, multiplexing of 3 FLIM-probes targeting spatially overlapping cell surface targets localized to the plasma membrane. Multiplexing capacity is then extended to 4 FLIM-probes within a single spectral channel, eliciting challenges of

non-specific signal. Finally deep learning applied to phasor analysis provides unbiased and systematic dimensional reduction, resolving false positive signal and standardizing a scalable approach for future increases in multiplexing capacity, **Fig. 2.1**.

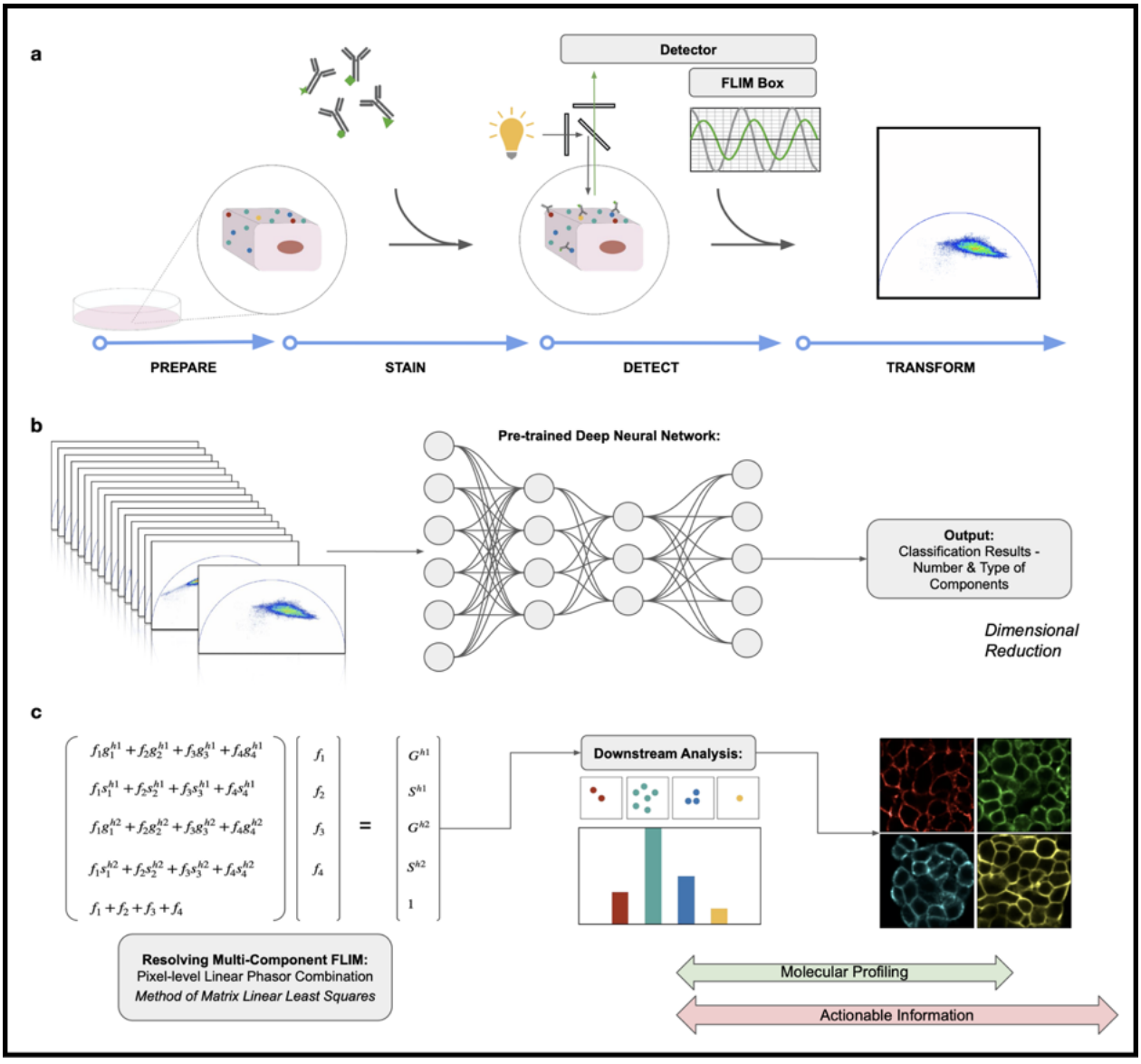

Figure 2.1: Schematic Overview of Multiplexed Workflow and Analysis.(a) Illustrates experimental steps in sample preparation, probe staining, collection of lifetime and harmonic information, and plotting pixel lifetimes on the phasor plot. (b) Input of processed phasor images into a trained ANN model to predict number and type of fluorescent species present. (c) Output of ANN used to reduce dimension of the linear system and subsequent resolution of intensity signals via phasor analysis.

2.2 The Phasor Approach to Fluorescence Lifetime Imaging Microscopy (FLIM)

Molecular absorption of energy results in excitation to higher energy levels. Newly excited molecules can return to ground-state through a number of different relaxation pathways including thermal relaxation, fluorescence, dynamic quenching, or other forms of non-radiative decays. In the fluorescent pathway, energy is released though the emission of light with characteristic properties dependent on the amount of energy being released. The field of fluorescence microscopy exploits these fluorescent properties of certain molecules (fluorophores) to investigate the molecular environment of cells and tissues. Histogram counts of photon arrival times following an excitation pulse and subsequent fluorescence emission decay exponentially. Fluorescence lifetime is an intrinsic property describing the duration of time required for an excited state fluorophore to decay to $\frac{1}{e}$ ($\approx$36.8%) of its original fluorescence intensity. For a singular exponential decay, this can be expressed mathematically by **Eq. 2.1**. However, if the decay is multi-exponential or composed of multiple independently contributing fluorescent species, it can be represented as a sum of exponentials, generalizing the expression to **Eq. 2.2**.

$$I(t) = I_0 e^{-t/\tau} \tag{2.1}$$

$$I(t) = \sum_{n=1}^{N} A_n e^{-t/\tau_n} \tag{2.2}$$

Fluorescence lifetime can be measured in the frequency domain by the application of a repetitive intensity modulated excitation light to a sample of interest, and subsequently measuring the fluorescence emission. The pattern of repetition of the excitation light can be deconstructed into a set of sinusoidal waveforms, each component of which will also be present in the emission signal. Analysis of the amplitude differences and phase shift in

these sinusoids can be used to determine fluorescence lifetime. This transformation is represented by **Eqs. 2.3** where m is the modulation ratio and ϕ is the phase delay. In the time-domain this is represented by **Eqs. 2.4** where n is the harmonic frequency and ω is the angular repetition frequency of the laser, ($\omega = 2\pi f$). The result is a Fourier series expansion of fluorescence signal into $g_{i,j}$ and $s_{i,j}$ values that represent lifetime as vector coordinates on a phasor plot. Importantly, as a result of the linearity of the Fourier analysis, vectors in the phasor space follow a law of linear combination. Moreover, the phasor approach to FLIM is reciprocal in nature, meaning spatial and temporal qualities of pixels are linked. For example, selection of pixels clustered by similar lifetime can be located in an image despite spatial separation.

$$g_{i,j}(\omega) = m_{i,j}cos(\phi_{i,j}) \qquad s_{i,j}(\omega) = m_{i,j}sin(\phi_{i,j}) \tag{2.3}$$

$$g_{i,j}(\omega) = \frac{\int_0^T I_{i,j}(t)cos(n\omega t)dt}{\int_0^T I_{i,j}(t)dt} \qquad s_{i,j}(\omega) = \frac{\int_0^T I_{i,j}(t)sin(n\omega t)dt}{\int_0^T I_{i,j}(t)dt} \tag{2.4}$$

As previously noted, for samples containing more than one independent fluorescent species, multi-exponential decays are derived from the sum of individual exponential decays describing each species. Determining fractional contribution of independent fluorescent species to the lifetime of a pixel relies on the linear relationships in the phasor domain. Previously reported work has demonstrated fractional lifetime resolution of up to 4 different fluorescent species in an individual pixel[60]. A system of 4 components results in linear combination of 4 exponential decays shown in **Eq. 2.5**. Fractional contribution of each component is defined by **Eqs. 2.6** and the sum of fractions cannot exceed unity. Therefore, phasor coordinates of each pixel in an image are described generally as the weighted sum of the lifetime coordinates of each contributing fluorescent component and

their respective fractional contribution within a pixel, **Eqs. 2.7**.

$$I(t) = A_1 e^{-t/\tau_1} + A_2 e^{-t/\tau_2} + A_3 e^{-t/\tau_3} + A_4 e^{-t/\tau_4} \tag{2.5}$$

$$f_n = \frac{A_n \tau_n}{\sum_{n=1}^{N} A_n \tau_n} \qquad \sum_{n=1}^{N} f_n = 1 \tag{2.6}$$

$$g(\omega) = \sum_{n=1}^{N} f_n g_m(\omega) \qquad s(\omega) = \sum_{n=1}^{N} f_n s_m(\omega) \tag{2.7}$$

The result is a system of equations for every pixel in an image describing the linear combination of independent lifetime component coordinates and their respective fractional contributions, **Eqs. 2.8-2.12**. The unknown fractional lifetime contributions for each pixel, f_i can be analytically determined using standard matrix linear algebra. Furthermore, due to the orthogonality of the Fourier expansion, collection of each additional harmonic (n) affords the necessary information to resolve additional unknown lifetime fractions, providing a basis for additional multiplexing capacity (M_c), described in **Eq. 2.13**.

$$f_1 g_1^{h1} + f_2 g_2^{h1} + f_3 g_3^{h1} + f_4 g_4^{h1} = G^{h1} \tag{2.8}$$

$$f_1 s_1^{h1} + f_2 s_2^{h1} + f_3 s_3^{h1} + f_4 s_4^{h1} = S^{h1} \tag{2.9}$$

$$f_1 g_1^{h2} + f_2 g_2^{h2} + f_3 g_3^{h2} + f_4 g_4^{h2} = G^{h2} \tag{2.10}$$

$$f_1 s_1^{h2} + f_2 s_2^{h2} + f_3 s_3^{h2} + f_4 s_4^{h2} = S^{h2} \tag{2.11}$$

$$f_1 + f_2 + f_3 + f_4 = 1 \tag{2.12}$$

$$M_c = 2 \cdot n + 1 \tag{2.13}$$

Thus far, a method to analytically resolve fractional lifetime contributions across every pixel in an image has been described. However, in order to extend phasor analysis to

FLIM-based multiplexed molecular imaging, translation of lifetime information to target-specific and quantitative fluorescent signals for each fluorescent species is necessary. Similar to standard immunofluorescence microscopy, specificity of molecular targeting relies on conjugation of distinct fluorescent species to antibodies targeting markers of interest. Leveraging these receptor-ligand affinities maintains modular and customizable production of exogenous molecular probes (FLIM-probes). Lifetimes of FLIM-probes are measured experimentally enabling pixel resolution of fractional lifetime contributions. Quantitative signal intensity for each FLIM-probe is then determined by the product of image intensity and resolved lifetime fractions. The result delineates marker-specific intensity from original, cumulative image intensity, into separate channels for each contributing probe respectively, **Eq. 2.14**.

$$I_{i,j} = f_n \cdot I^0_{i,j} \tag{2.14}$$

These reconstructed intensity images for each FLIM-probe ultimately recover probe-specific immunofluorescence and resulting marker expression analogously to imaging using spectrally distinct probes. Importantly, this algorithmic, fit-free approach simplifies workflows by capturing signal intensity for up to 4 simultaneously employed probes. Concurrent staining of all probes circumvents cyclic staining requirements, spatial registering and alignment of sample, or otherwise degradative techniques needed when capturing multiplexed signal within a single spectral band. In addition, resolving all probe targets reduces the need to prioritize target selection due to limited multiplexing capacity. This platform technology enables capture of multiplexed molecular expression, irrespective of a-priori information of sample content.

2.3 Resolution of 3 Spatially Separated Targets

As an initial demonstration of fluorescence lifetime based molecular multiplexing, 3 spatially separated cellular markers (surface, cytoplasmic, and nuclear) were simultaneously targeted, imaged, and resolved using 3 spectrally overlapping but temporally distinct FLIM-probes. Epithelial cell adhesion molecule (EpCAM) is both plasma membrane specific and commonly over-expressed in many cancer phenotypes. Cytokeratin (CK) is a prominent cytoskeletal component of epithelial tissues with cytoplasmic distribution. Lastly, Ki-67 is a nuclear marker indicative of proliferative state and therefore cellular presence is clinically indicative of carcinoma. Spatial separation of cellular targets provides a facile means of evaluating analysis accuracy and recovery of marker specific signal intensity. Direct comparison of resolved probe localization with expected cellular distribution makes misallocated signal markedly apparent. Moreover, development of spatially resolved multiplexing enables direction benefits of FLIM to molecular trafficking studies.

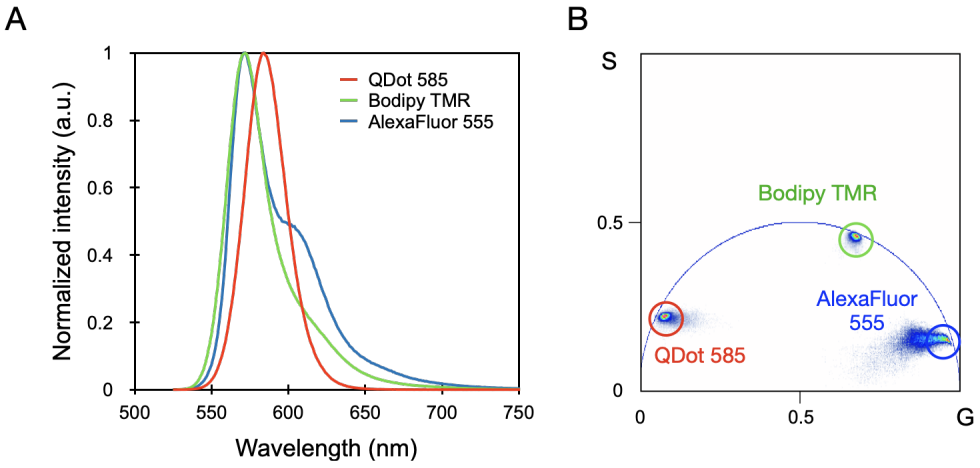

Figure 2.2: Spectral Overlapping and Temporally Distinct Fluorescent Species. (A) Normalized spectral emission data of 3 different fluorescent species (QDot 585, BodipyTMR, AlexaFluor 555) indicating significant overlap. (B) Combine phasor plot of 3 independent MCF7 cell samples stained with a different FLIM-probe, illustrating distinct temporal properties.

Three spectrally overlapping fluorescent species (Quantum Dot 585, BodipyTMR and Alexa Fluor 555) with distinct fluorescent lifetimes were chosen to develop molecular FLIM-probes targeting the three spatially separated cellular markers. Fluorescent species were conjugated to monoclonal antibodies targeting the 3 spatially separated markers (EpCAM, CK, and Ki-67) respectively. In-vitro samples of human breast cancer cell line (MCF7) were first stained with each single probe individually to experimentally capture pure species lifetimes. The measured emission spectra of the three species in solution were plotted illustrating large overlap of emission within the 550-650nm range **Fig. 2.2A**. In addition to spectral overlap and distinct lifetimes, fluorescent species were chosen for ample euclidean separation and linear orthogonality on the phasor plot. During lifetime imaging, samples were excited at 534nm and fluorescence emission was collected between 560-660nm, averaging photon counts for each pixel over 50 collected frames. Lifetime signals were recorded, transformed, median filtered, and plotted on the phasor. The effect of median filtering is a lossless method to de-noise data that maintains resolution. The phasor data from each experiment was combined into a single phasor plot for comparison, demonstrating extent of temporal separation **Fig. 2.2B**. Colored circles (red, green, blue) highlight locations of each pure FLIM-probes and match color coding of spectral data. Among all spectrally-matched, long-lifetime fluorescent species surveyed, the three chosen exhibited the greatest degree of orthogonality and separation with respect to each other. In addition, plotting lifetimes on the same phasor enabled rapid visual confirmation that phasor locations correlated with expectations from previous solution-based measurements of the unconjugated fluorescent species. This suggests lifetimes remain distinct and largely unchanged irregardless of bio-conjugation, indicating FLIM-probes can be engineered in a "plug-and-play" manner for multiplexing by coupling temporally distinct fluorescent species to antibodies targeting markers of interest.

Next, single-probe stained images were used to compute 2D histograms of collected pixel lifetime coordinates across two harmonics. The coordinate bins with maximum counts

were used to identify the single pure component coordinates in each harmonic and used as a basis for constructing the linear system of equations. Although single harmonic information is sufficient for multiplexing 3 probes, use of the second harmonic nets an overdetermined system providing improved signal fidelity. Using this information, intensity images were reconstructed for each probe channel in the single-stained experiments. Images in **Fig. 2.3** show original total intensity followed by the phasor and three reconstructed image channels corresponding to the three probes employed. Images were normalized and pseudo-colored to match the colored circles on the phasor. Original intensity images confirmed specific fluorescent staining of the three cellular compartments for each probe-target pair, with high signal-to-noise and minimal autofluorescence. Resulting signal in reconstructed images also correctly correspond to the target marker and match original intensity images, demonstrating resolution of signal intensity using lifetime information.

Additional samples were then stained and imaged with all 3 FLIM-probes together. Intensity and lifetime data were analyzed and resolved into separate image channels, **Fig. 2.4**. Expectedly, as a result of spectral overlap, probe-specific information in original intensity images, **Fig. 2.4(i)**, are indistinguishable and agnostic to cellular marker identity when relying on spectral information alone. Although using three different spectral probes could easily achieve the intended separation, spectral overlap and crosstalk limit further multiplexing capacity. Alternatively, lifetime data provides another dimension to multiplex within each spectral band and is complementary to standard spectral approaches. The lifetime of pixels are plotted on the phasor, **Fig. 2.4(ii)**, and the colored circles indicate the positions of the pure probe species. Pixel locations are expected to fall within a triangle formed depending on the linear combination of fractional lifetime from each of the three pure species, with the colored circle positioned at the vertices. Here the distribution of pixel lifetimes fall within the demarcated region defined by the three pure probe locations. Phasor distributions of multiplexed images appear densest between red and green circles primarily due to a larger fraction of the cell and therefore positively stained image pixels

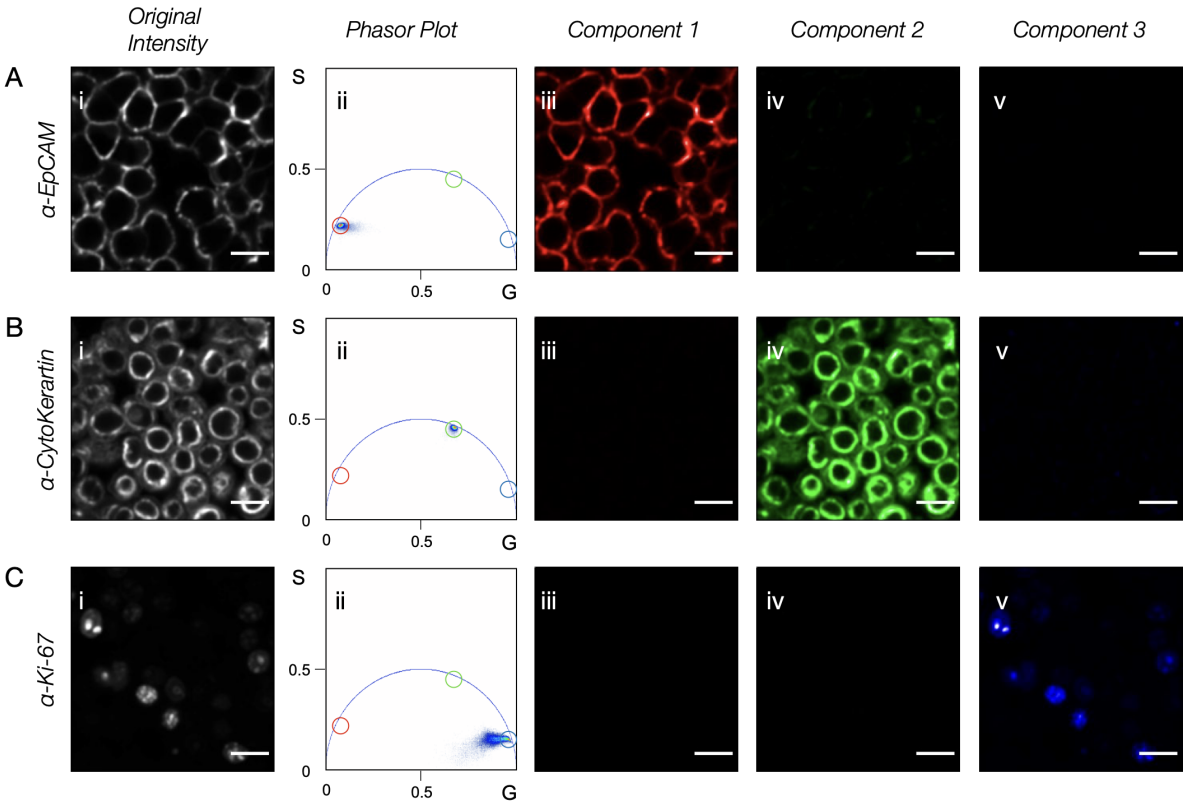

Figure 2.3: Spatially Separated, Single-Probe Stained MCF7 Cells. (A-C) MCF7 cells stained with FLIM-probes targeting EpCAM, Cytokeratin, and Ki-67 respectively. (i) original total intensity images, (ii) corresponding first harmonic phasor plots, laser frequency=20MHz, and (iii-v) resolved and reconstructed component-specific fluorescence images after phasor analysis. Scale bars=20μm.

for these two targets. Moreover, pixels positioned at the membrane-cytoplasmic interface are likely to span cellular regions where both membrane and cytoplasmic markers can be found. This marker overlap results in pixels containing various fractional combinations of two fluorescent components causing phasor distributions to fall between the two pure probes for these targets. Pixels beyond the peri-nuclear region likely containing solely nuclear targets, spatially distinct enough from the other two cellular compartments, making it unlikely to contain more than a single fluorescent component. Therefore a second, mostly isolated cluster of pixels appear near the blue circle on the phasor. In summary, few pixels are likely to contain all 3 components simultaneously. Interestingly, the reconstructed images, **Fig. 2.4(iii-v)**, resolve signal by stained cellular compartment.

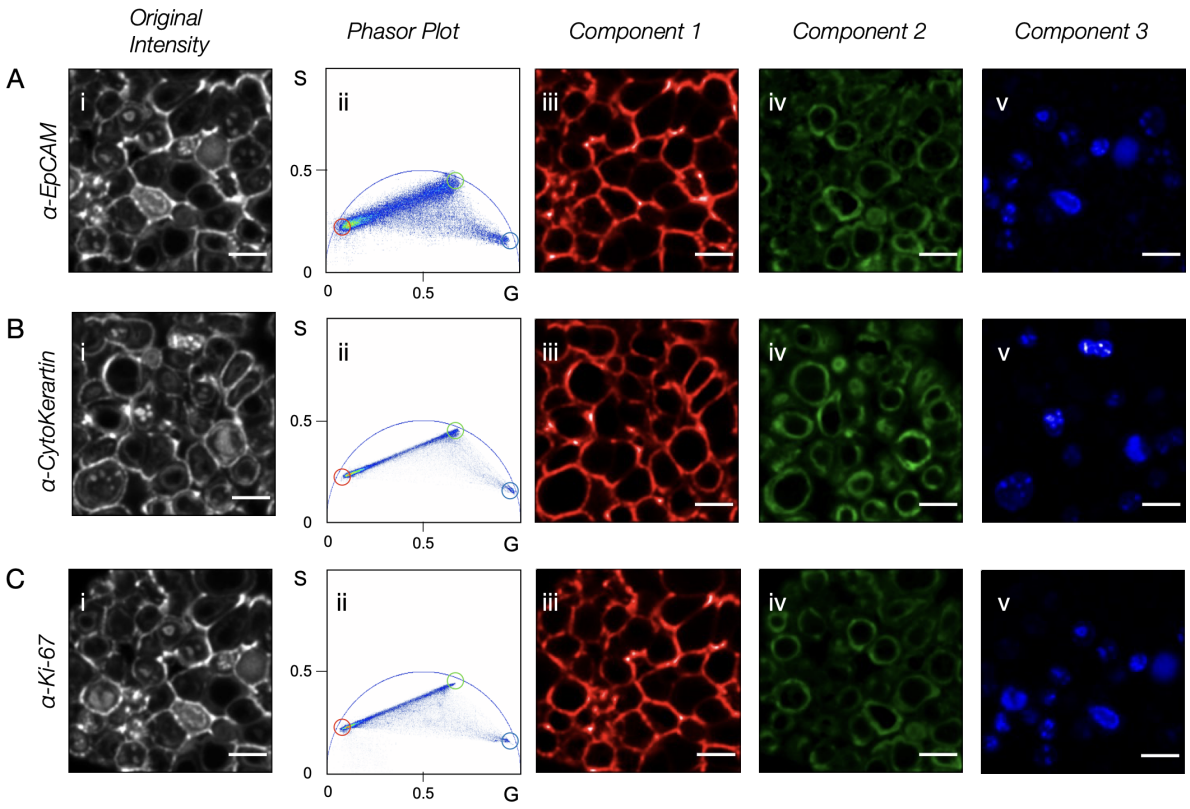

Figure 2.4: Spatially Separated, 3-probe Multiplexed MCF7 Cells. (A-C) Replicates of MCF7 cells stained with all FLIM-probes targeting EpCAM, Cytokeratin, and Ki-67 simultaneously. (i) original total intensity images, (ii) corresponding first harmonic phasor plots, laser frequency=20MHz, and (iii-v) resolved and reconstructed component-specific fluorescence images after phasor analysis. Scale bars=20μm.

EpCAM signal is confined to the membrane surface, cytokeratin signal is cytoplasmic in distribution, and Ki-67 signal is confined within the nucleus. The results match expected cellular distribution of the three target markers and non-specific signal is not visually apparent in alternate channels suggesting successful delineation of probe-specific signal intensity. A composite pseudo-colored image was generated to highlight the comparison of results to standard multiplexed immunofluorescence techniques that rely on spectral band resolution. However, here results were ultimately generated from a single sample employing all 3 FLIM-probes simultaneously and resolved solely based on fluorescence lifetime, demonstrating the phasor approach to multiplexed molecular imaging, **Fig. 2.5**.

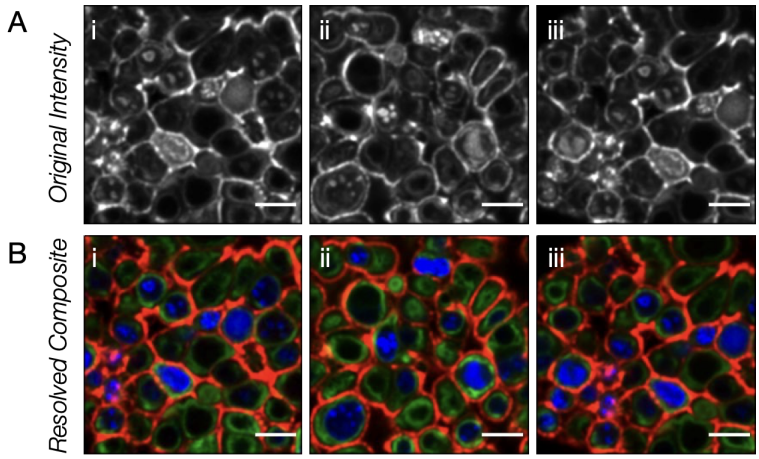

Figure 2.5: Lifetime Resolved, 3-probe Spatially Multiplexed Composites. (A) Original total intensity images from 3 experimental replicates collected from a single spectral window. (B) Pseudocolored images for EpCAM (red), Cytokeratin (green), Ki-67 (blue) resolved solely using fluorescence lifetime. Scale bars=20μm.

2.4 Resolution of 3 Spatially Co-localized Targets

The translational value of multiplexed high-content imaging modalities is the ability to rapidly and quantitatively elucidate numerous molecular indicators of normal and diseased, yet intact, cellular environments while maintaining morphologically defining features. Simultaneous acquisition of data can eventually provide contextualized actionable information with applications ranging from identification of current or novel drug targets, observation and characterization cell-cell interactions, or guiding clinical diagnoses and management. In particular, membrane bound surface markers are gateways for cell signaling and transduction pathways, and therefore informative and potentially druggable targets. However, the membrane surface is heterogeneous and fluid meaning many targets of interest overlap or coexist in spatial proximity. As a result elucidating the molecular heterogeneity present even within the confines of the membrane surface makes multiplexing of co-localized molecular targets a difficult, yet important feature of accurate, specific, and sensitive high-content imaging modalities. Additionally, variability in receptor expression intrinsically distinguishes normal versus pathological cell types and states, providing

further basis as prognostic and therapeutic targets. Epithelial cell adhesion molecule, epithelial cadherin, and transferrin receptors are common epithelial surface markers with broad oncogenic, diagnostic, and/or prognostic value as neoplastic signatures of breast cancer or as hallmarks of metastasis (epithelial-to-mesenchymal transition). Molecular sub-typing is also particularly clinically relevant in the specific management of neoplastic pathologies of the breast. Not only is the lack of E-Cadherin (ECad) common in invasive lobular carcinomas, a subset of breast cancers exhibit and are classified by over-amplification of human epidermal growth factor 2 (HER-2). HER-2 positive breast cancer is responsive to treatment with trastuzumab, underscoring the importance of characterizing molecular phenotype.

The molecular landscape of cellular environments is rich in variety, organization, and function. While multiplexing spatially distinct targets is necessary, the abundance of key molecular drivers of disease are often active at the membrane surface and therefore extension of spatial multiplexing Is required to capture of this rich information. To demonstrate the ability to multiplex co-localized targets, additional FLIM-probes targeting different, spatially co-localized, epithelial cell surface biomarkers were assembled. Each of four fluorescent species (QDot 585, KU530, BodipyTMR, and AF555), **Fig. 2.6A** were conjugated to monoclonal antibodies against epithelial cell adhesion molecule (EpCAM), human epidermal growth hormone receptor 2 (HER-2), epithelial cadherin (E-Cad), or transferrin receptor (TfR) respectively.

To demonstrate reproducibility of lifetime and specificity of molecular targeting, human breast cancer cell lines (Bt474, ATCC) were stained with the epithelial FLIM-probes and each single-stained sample was imaged. Bt474 cells were chosen as a model cell line due to high expression of each of the four markers, previously confirmed by flow cytometry. Fluorescence intensity images from each experiment, **Fig. 2.6B (i-iv)**, confirmed specific fluorescent staining of the cellular membrane surface for each

probe-target pair, with high signal-to-noise and minimal autofluorescence. Once again as a result of spectral overlap, original intensity images are indistinguishable and agnostic to surface marker identity when relying on spectral information alone. Typically, the use of specialized techniques or equipment such as cyclic staining and antigen retrieval methods or hyper-spectral cameras are needed to resolve these otherwise indistinguishable differences. The phasor data corresponding to the fluorescence images were plotted on the combined phasor, **Fig. 2.6C**. The results make the intrinsic and temporally distinct character of the probes apparent, highlighting lifetime as an independent dimension for multiplexing.

First, epithelial probes conjugated to each of the 3 fluorescent species (QDot 585, BodipyTMR, and AF555) used in spatially separated studies were used to demonstrate 3-probe multiplexing because of their ideal characteristics. The combination of separation of lifetime as visualized on the phasor, minimal complexity reflected by proximity to the universal circle, and minimal pure species variance when employed in cellular contexts make them ideal for multiplexing within the same spectral window. Human breast cancer cell line (Bt474) cells were chosen as a model cell line due to high expression of each of the three markers, previously confirmed by flow cytometry. Samples were stained with up to a

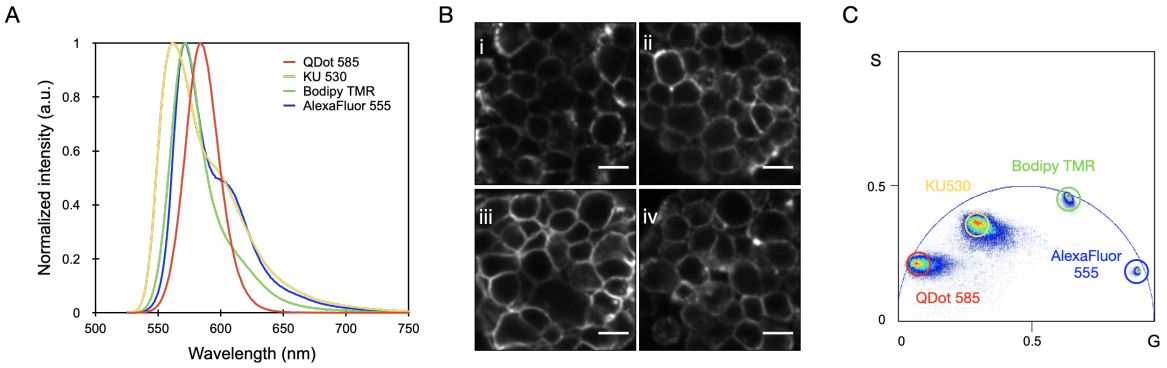

Figure 2.6: Development of 4 Spectral Overlapping and Temporally Distinct Epithelial FLIM-Probes. (A) Normalized spectral emission data of 4 different fluorescent species (QDot 585, KU530, BodipyTMR, AlexaFluor 555) indicating significant overlap. (B) Intensity images of each single-probe stained Bt474 cell sample (C) Combine phasor plot of 4 independent Bt474 cell samples stained with a different FLIM-probe, illustrating distinct temporal properties. Scale bars=20μm.

total of 3 FLIM-probes to to capture all 7 possible combinations of 1-, 2-, and 3-probe staining conditions. Experiments were performed to demonstrate the robustness of multiplexed targeting of spatially co-localized cell surface markers.

The intensity and lifetime signals were recorded, transformed, median filtered, and plotted on the phasor. Using lifetime information, intensity images were reconstructed for each staining condition analogous to traditional three-color immunofluorescence microscopy. Images in **Fig 2.7** show original total intensity followed by the phasor and three reconstructed image channels corresponding to the three probes employed in single-probe staining conditions. Images were normalized and pseudo-colored to match the colored circles (magenta, yellow, green) on the phasor which refer to pure species lifetime locations of the 3 epithelial FLIM-probes targeting EpCAM, ECad, and TfR respectively. Signal for each probe in reconstructed images are specific to the cellular membrane and present in only the expected probe specific channel.

Original intensity images of dual-probe and triple-probe stained samples are uninformative of molecular identity as a result of spectral overlap, **Fig 2.8 (i)**. However, on the phasor plots the lines connecting the colored circles in 2-probe stains indicate the expected trajectory of pixels containing a range of linear combinations of fractional lifetime of each of the two pure species, **Fig. 2.8 (ii)**. For pixels containing two fluorescent components, the euclidean distance between the pixels and a pure species is indicative of the degree to which that species contributes to the pixel's lifetime. The smaller the distance, the larger the "pull" a pure species has, and the larger the lifetime fraction of a pixel originates from that pure species. Since targets are coexistent within the same membrane surface, a large fraction of pixels will contain both probes with varying fractional content of each.

This manifests with phasor distributions of 2-probe stained image pixel lifetimes appearing as a streak of pixels falling linearly between the two pure probe locations rather

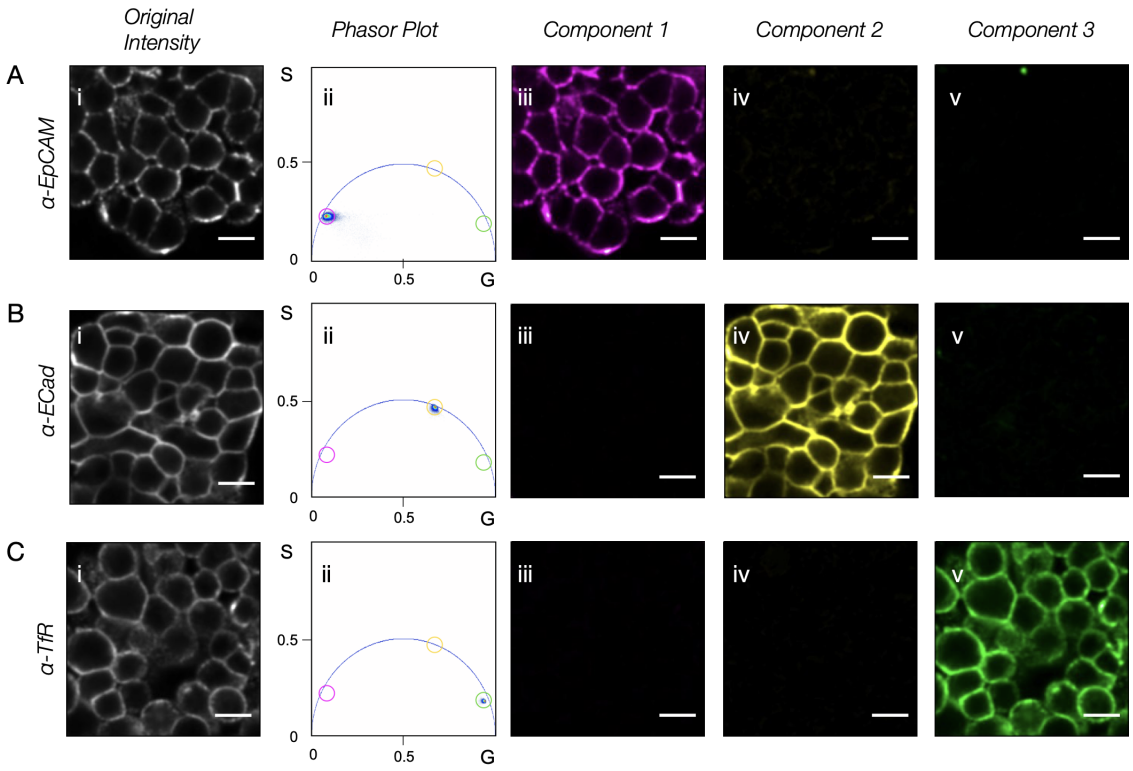

Figure 2.7: Spatially Co-localized, Resolved Single-Probe Targeted Bt474 Cells. (A-C) Bt474 cells stained with FLIM-probes targeting EpCAM, ECad, and TfR respectively. (i) original total intensity images, (ii) corresponding first harmonic phasor plots, laser frequency=20MHz, and (iii-v) resolved and reconstructed component-specific fluorescence images after phasor analysis. Scale bars=20μm.

than isolated clusters. The linearity also suggests absence of interaction or energy transfer between the probes despite targeting co-localized regions. Photo-physical interaction such as energy transfer, would otherwise manifest as loss of linearity in the pixel distribution and require accounting for quenching and excitation effects of a donor acceptor pair, further complicating resolution of fractional lifetime contributions. The triangles connecting the colored circle in the 3-probe stained image phasor once again indicate the expected locations of pixels with varying fractional content of three components with pure species located at the vertices. The majority of experimental pixel lifetimes fall within the demarcated region. The identified pure component coordinates, from maximum 2D histogram counts of single-stained images were used to construct the linear system of equations. The three reconstructed image channels corresponding to the three probes

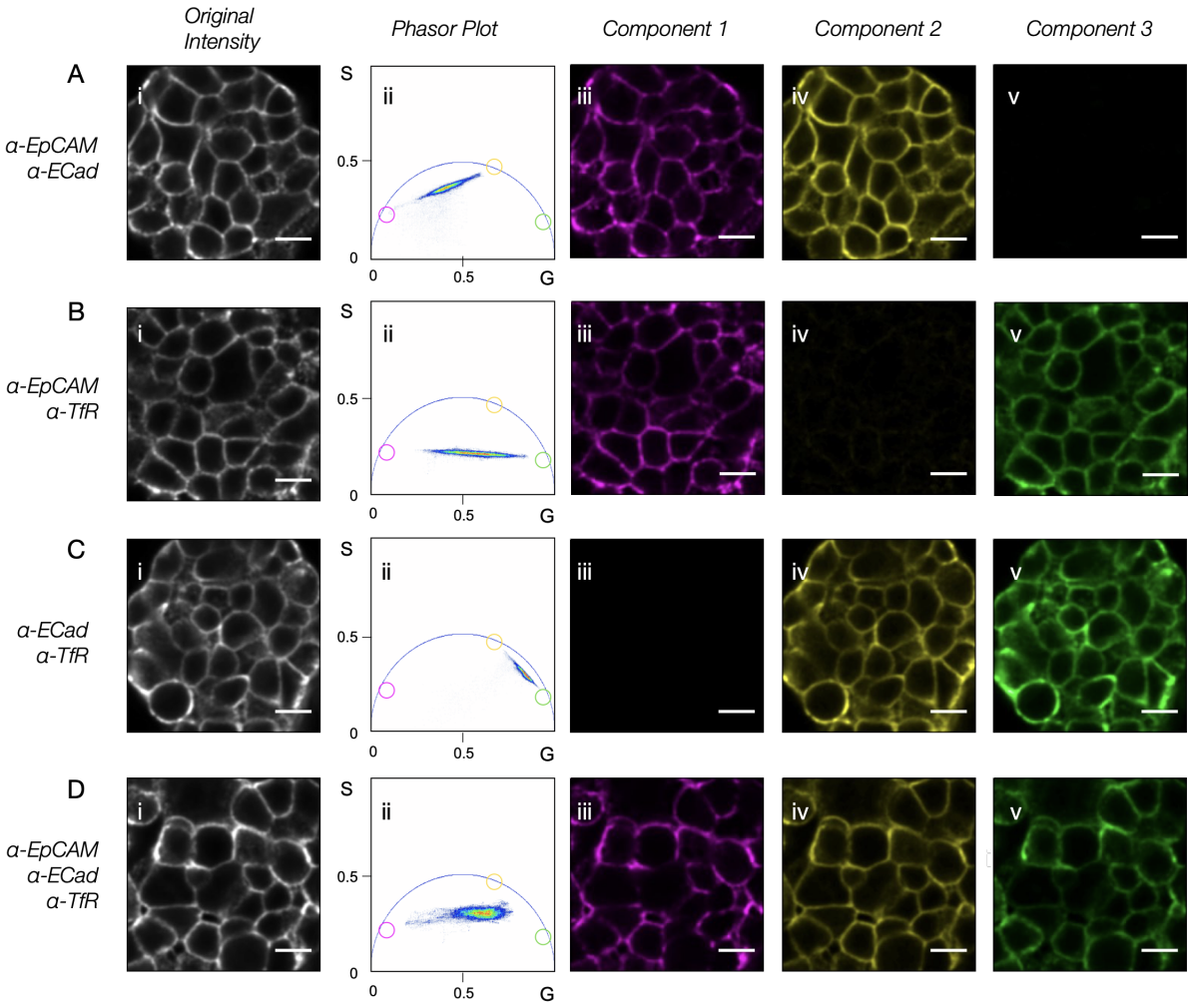

Figure 2.8: Spatially Co-localized, Resolved Dual-Probe and Triple-Probe Targeted Bt474 Cells. (A-C) Bt474 cells stained with combinations of 2 FLIM-probes targeting EpCAM, ECad, and TfR respectively. (D) Bt474 cells stained with all 3 FLIM-probes targeting EpCAM, ECad, and TfR (i) original total intensity images, (ii) corresponding first harmonic phasor plots, laser frequency=20MHz, and (iii-v) resolved and reconstructed component-specific fluorescence images after phasor analysis. Scale bars=20μm.

employed in an experiment are shown in **Fig. 2.8 (iii-v)**. Images were normalized and pseudo-colored to match the colored circles on the phasor. Signal for 2-and 3-probe stained images fall within the expected channel for the probes employed in each case while maintaining cellular morphology and specificity to the membrane surface.

While images are qualitative and visually informative, quantifying signal intensity provides relative expression of the targeted markers. The intensity distributions of

reconstructed images for all staining scenarios are transformed and violin plots are generated in **Fig. 2.9**. The data suggests distributions are similar across a specific probe-type. More importantly, interquartile ranges are similar in size and dispersion with mostly normal skew, further highlighting comparable recovery of multiplexed marker specific signal with standard single-probe measurements. The violin plot of the 2-probe case simultaneously targeting EpCAM and TfR, indicates small (5%) false positive signal in the ECad channel. The result is minimal and partially a result of the discrete nature by which pure component lifetimes are identified. Mean image intensity for reconstructed images across each staining condition are plotted in **Fig. 2.10**. Mean intensity of original single stains (gray bar) is a reference directly equivalent to standard immunofluorescence imaging. Comparing to mean signal intensities of reconstructed images within a single probe channel for all 2-and 3-probe stains demonstrates the phasor analysis correctly and quantitatively recovers signal within standard error, and true positive and negative conditions are easily discriminated. These results demonstrate not only the capability to multiplex spatially co-localized exogenous molecular probes within the same spectral channel, but to do so quantitatively using lifetime information alone. Recovery of quantitative, probe-specific fluorescence intensity enables comparison to fluorescence calibration curves and eventually relative recovery of marker expression. Moreover, this approach enables future multiplicative increases in multiplexed imaging by the addition of unique probes within a spectral channel and employing probes across other spectral windows in parallel.

2.5 Resolution of 4 Spatially Co-localized Targets

As a further demonstration of FLIM-based multiplexed molecular imaging, all 4 independent molecular FLIM-probes were assessed simultaneously. Bt474 cells were stained using all 15 possible combinations of 1-, 2-, 3-, and 4-probes. Images were analyzed,

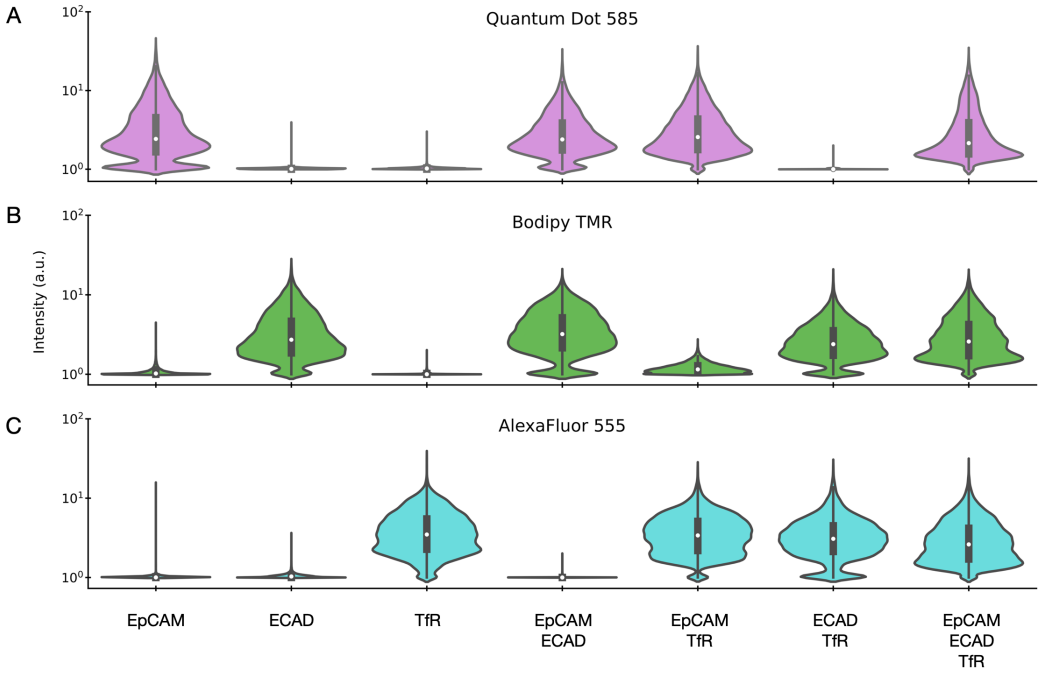

Figure 2.9: Intensity Distributions of Multiplexed Spatially Co-localized Bt474 Cells. (A-C) Violin plots of individual resolved images from various experimental probe staining conditions according to EpCAM, ECad, and Tfr channels respectively.

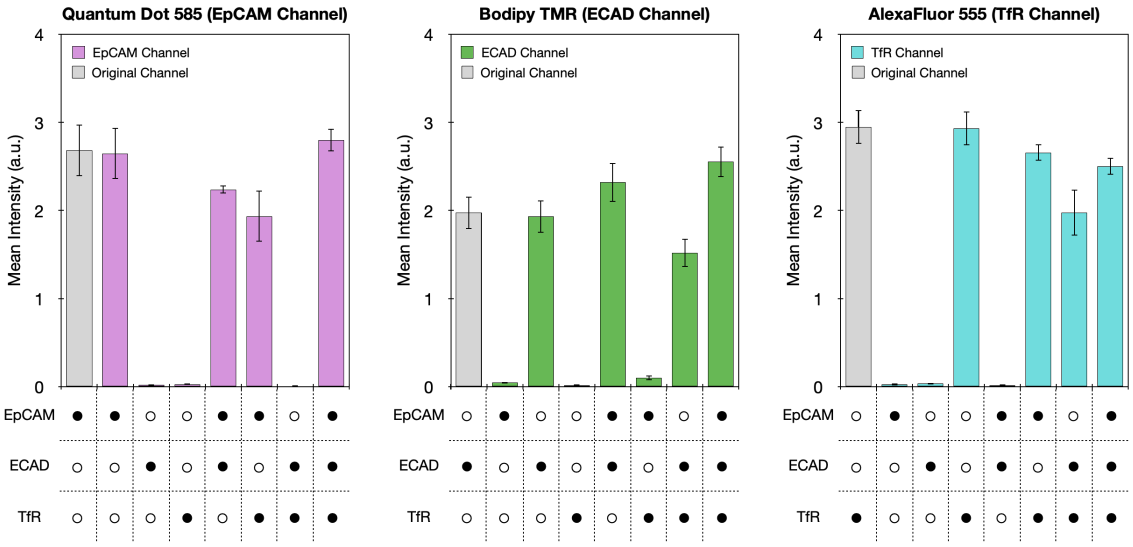

Figure 2.10: Mean intensity of probe-specific multiplexed channels. (Left) Mean intensity of resolved EpCAM channel images. (Middle) Mean intensity of resolved ECad channel images. (Right) Mean intensity of resolved TfR channel images. Means calculated as Grand Mean of mean image intensity across 3 replicate conditions.

resolving fractional lifetimes to reconstruct probe-specific intensity images. However, while analysis attributes resolved image signal intensity to the expected probe-specific channels, sparse and punctate signal also surfaced in unstained channels. Moreover, signal originating from the KU530 probe is modest and noisier as a result of reduced relative brightness compared to the other more robust fluorescent species employed. This observation was more quantitatively evident in violin plots of intensity distributions for all staining conditions, shown in **Fig. 2.11**. The data suggests phasor lifetime analysis with these 4 possible contributing probes results in false positive signal arising from "signal bleed through" from other channels. Broadly, this indicates the rank of linear system is inconsistent with the total number of probes involved. As a result, fractional lifetimes of pixels are not entirely linearly independent. Importantly, multiplexing only 3 probes affords ideal probe selection and placement to maintain linear independence so the effect is not realized. However, adapting the platform for multiplexing beyond 3-probe systems was expected to elicit a number of challenges.

The resulting sources of error made evident with a higher degree of multiplexing can be attributed to the effect of using discrete pure species lifetimes in cellular contexts, limitations of spectrally matched long-lifetime probe availability and the resulting partial loss of linear orthogonality between probe phasor locations. The currently limited availability of reliable, spectrally-matched, long-lifetime fluorescent probes makes selection of probes with unique, linearly orthogonal phasor locations a non-trivial task. KU530 provided the most orthogonal phasor location of the probes examined; however, complete orthogonality is not achieved in part by the diffuse lifetime distribution resulting in analytical ambiguity. Since the analysis depends on the analytical solution to a linear system of equations, a unique solution will be determined for a coefficient matrix of rank equivalent to the maximum number of probes employed. As a result, these effects of "signal bleed through" occur most notably when resolving all four channels for conditions

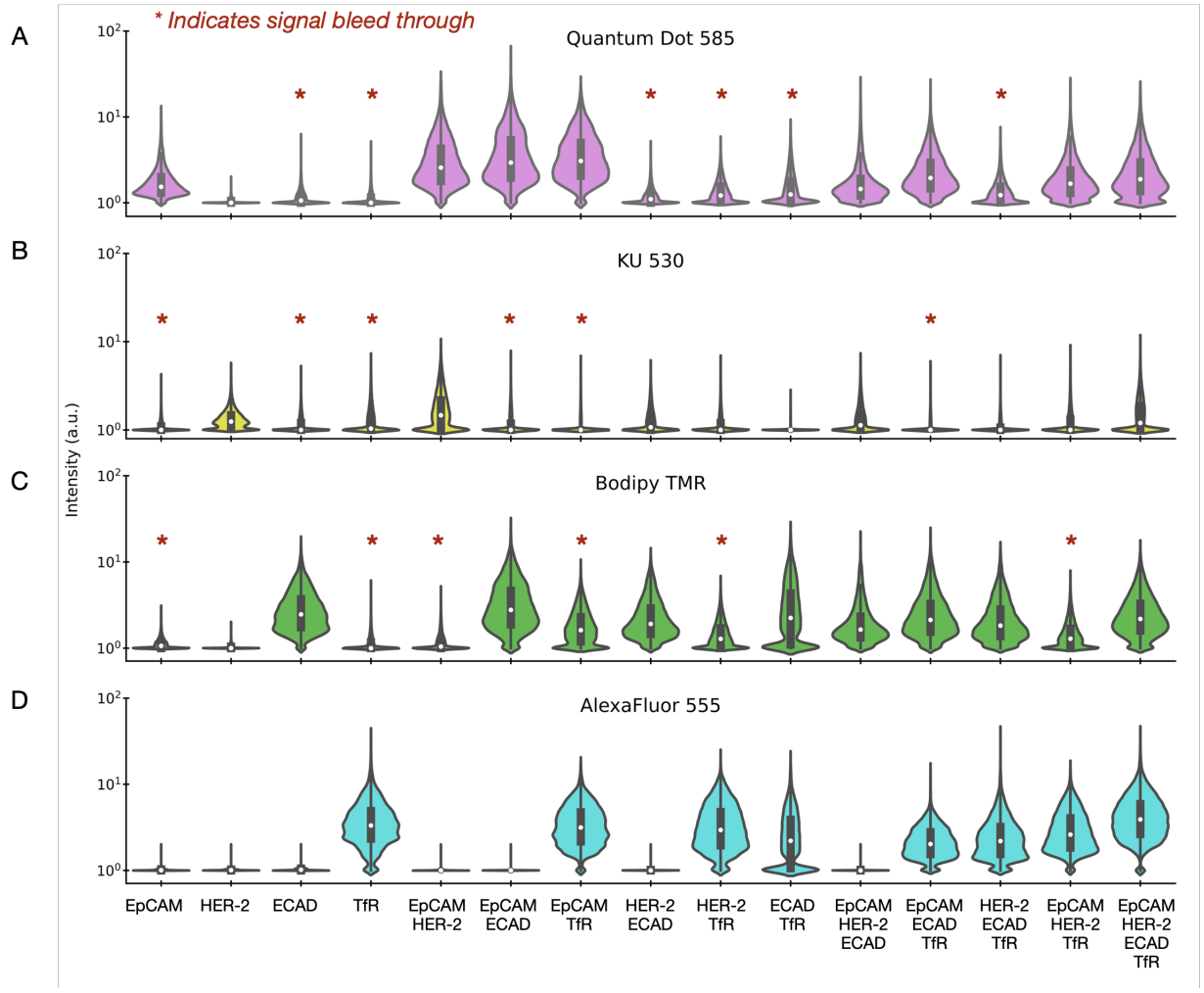

Figure 2.11: Intensity Distributions Across All 4-probe Multiplexed Studies. (A-D) Violin plots of individual resolved images from various experimental probe staining conditions without machine learning dimensional reduction according to EpCAM, HER-2, ECad, and Tfr channels respectively.

stained with fewer than 4 probes. As a result, the unstained components are attributed signal in order to arrive at a unique solution that maintains unity of fractional lifetime.

In conditions stained with fewer than 4 probes, the unstained channel becomes a negative control as its corresponding lifetime fractions cannot assume non-zero values. Although artificially engineered, such experimental conditions mimic potential variability of target marker expression across sample types of interest. For example, triple-probe stained samples are analogous to HER-2 negative samples, where cellular expression of 1 or

more molecular targets is absent. Therefore rather than resolving all 4 components, identification and classification of negative expression prior to fractional lifetime analysis facilitates variable elimination and reduction of linear system dimension. As a result, subsequent analysis reduces false positives by precluding attribution of signal in the negative or unstained channel. Moreover, as sample complexity grows, this feature would simplify potential future clinical utility of the platform, such as facile discrimination of HER-2 status and the resulting impact on therapeutic choice.

Having established need for dimensional reduction to complement phasor analysis, the question shifts to which methodology is best. Manual introduction of a-priori information for each sample would require additional data logging, introduces potential bottlenecks in computational speed, and is neither scalable or unbiased. More importantly, is not applicable when investigations are exploratory or sample identity is unknown. Instead, an automated, scalable, and unbiased approach for accurately classifying, predicting, and reducing the dimension of higher-order FLIM systems is more clinically tractable.

2.6 A Deep Learning Approach to Dimensional Reduction of Multi-Component Phasor Analysis

The phasor approach to FLIM is powerful in simplifying complex multi-exponential decays and representing lifetime mixtures in a geometric, graphical manner. As demonstrated, phasor distributions of systems containing multiple lifetime components predictably fall within geometric shapes with vertices defined by pure species lifetimes. As a result, trained personnel are able to intuit the number of components and therefore extent of multiplexing up to a certain extent through visual inspection, **Fig. 2.12**.

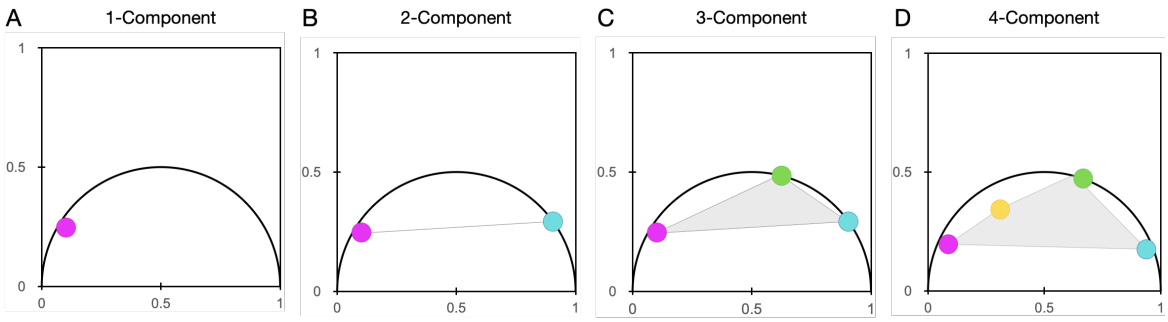

Figure 2.12: Schematic Phasor Plots of Different Multi-Component Systems. (A-D) Schematic demonstration of 1-, 2-, 3-, and 4-component systems respectively. Colored circles indicate pure component lifetime locations and shaded/connected regions indicate locations where pixel lifetimes are characteristically expected to fall.

Identification of these features enable dimensional reduction of phasor analysis. However, relying on trained personnel is not only costly, but is subject to human error, and will reach a threshold beyond which features are no longer discernible above noise by human perception. The field of machine learning applies a variety of statistical methods and algorithms to images for applications including object recognition, classification, and segmentation. Deep learning in particular relies on artificial neural networks (ANNs) for robust feature extraction and have been used extensively to build predictive models. ANNs are networks of nodes and connections inspired after biological neural networks of interconnected neurons. These networks are linear connections of signals and weights, and amplification or dampening of weights provide the learned and predictive power. These networks view images as vectors of discrete values which are cascaded through layers of feature extraction, ultimately outputting vectors containing probabilities of selected outcomes. Models trained on the publicly available MNIST images of handwritten numerical digits have accurately predicted the digit written in these images. The graphical nature of the phasor approach is analogously well-suited for supervised deep learning where labeled ground-truth images are used to train multi-class classification models capable of phasor pattern recognition. Such a supervised network could efficiently identify patterns in

information-rich lifetime data and reliably predict features to reduce the dimensionality of multiplexed systems with high accuracy in a scalable, unbiased manner.

However, one drawback is that supervised deep learning is a data-hungry approach. Large amounts of labelled data are necessary to train representative and accurate models. Accordingly, additional FLIM data was collected on multiple breast cancer cell lines stained with all combinations of 1-, 2-, 3-, and 4- probes to train and validate a deep learning classifier. Cell lines were chosen for variability of all four epithelial surface marker expression. In total 100 phasor images were captured, processed, and distributed by 65% and 35% into training or validation sets respectively. The various 2- and 3-probe phasor distributions of Bt474 cells highlight the variability and fingerprint-like signature phasors provide of different multiplexed conditions, **Fig. 2.14**. Additional phasor distributions from other cell lines along with implementation of dropout during model training prevented overfitting and improved generalizability of the model, reaching an accuracy of 95%, see Fig M. Ultimately, the deep learning model classifies fluorescence lifetime phasor patterns according to the number of pure species lifetimes present and surface markers actively targeted in a given experimental condition.

To investigate the effectiveness of the model in reducing "signal bleed through", the model was implemented to reevaluate resolution of 4 spatially co-localized surface targets. The addition of deep learning codified the evaluation of degree of multiplexing present by geometric phasor pattern recognition and subsequently simplified linear combination analysis of the 1-, 2-, 3-, and 4-probe stained Bt474 samples, by predicting the number and specific identity of probes present in a sample.

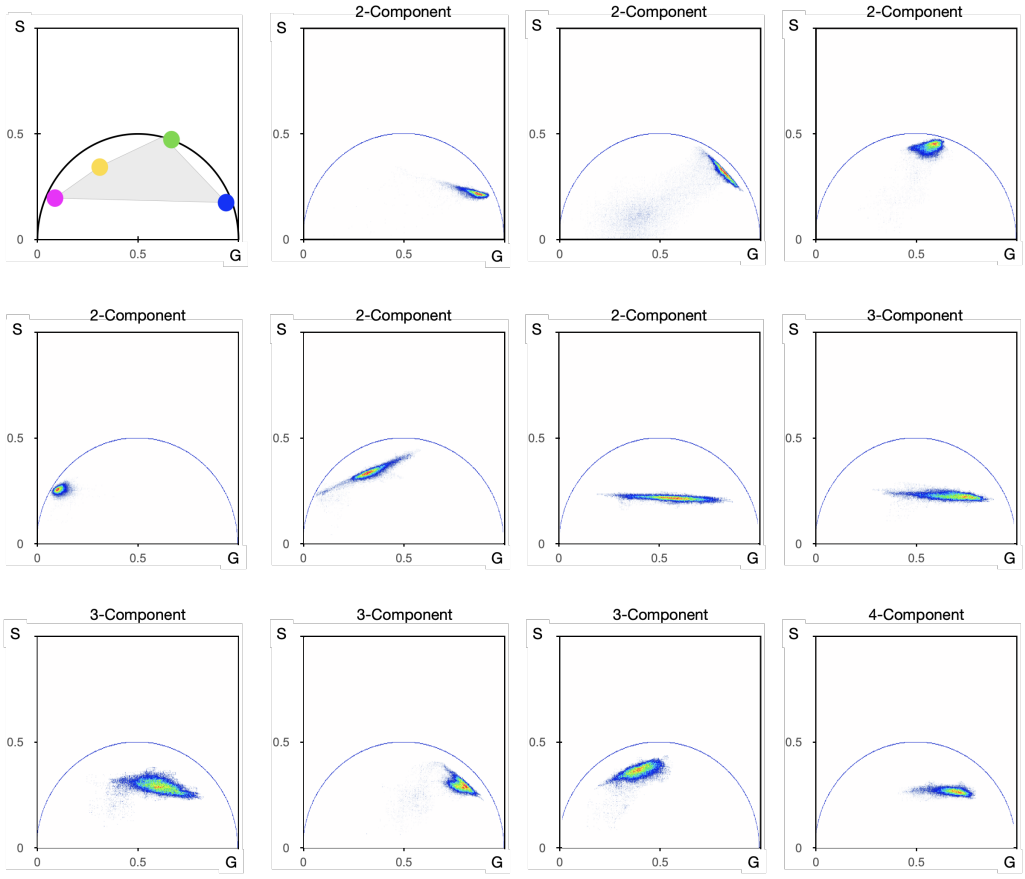

Figure 2.13: Different Multiplexed Experimental Phasor Plot Signatures. Collection of phasor plots from Bt474 cell samples stained with varying number and combinations of probes to highlight the graphical fingerprint-like nature of Phasor-FLIM.

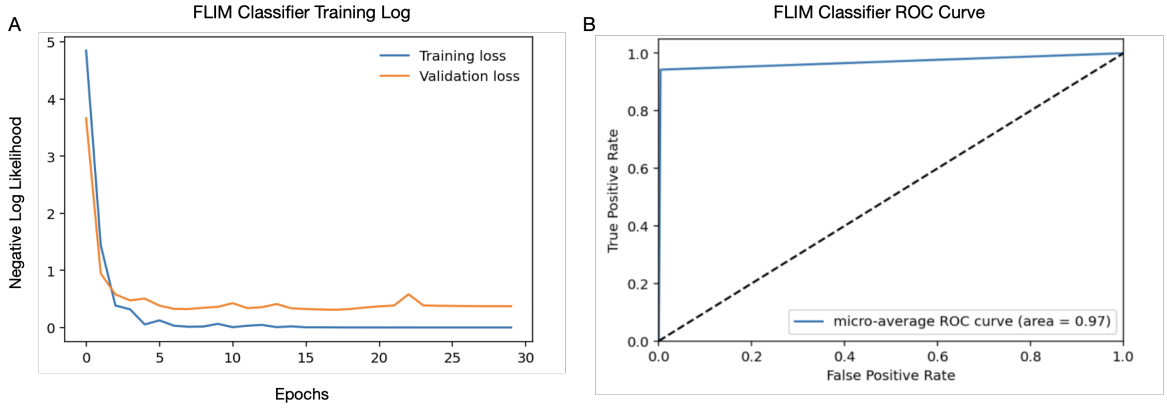

Figure 2.14: ANN Loss Curves and Multi-class ROC. (A) Model loss plotted for training (blue) and validation (red) over 30 epochs of batched training. (B) A multi-class ROC curve illustrating model accuracy above random (dashed line).

2.6.1 Resolution of Dual-Probe Stained Samples

The model was first implemented on phasors of dual-probe stained images. In each experiment, Bt474 cells were stained consecutively with 2 of 4 possible epithelial FLIM-probes prior to imaging. Experiments were arranged to comprise all six possible combinations of 2-probe staining conditions given the four previously conjugated probes (EpCAM-QD585, HER2-KU530, ECAD-Bodipy-TMR, and Tfr-AF555). The resulting 6 scenarios were imaged and lifetime signals were recorded, transformed, median filtered, and plotted on the phasor. Each panel in **Fig. 2.16(ii)** shows the phasors corresponding to each staining condition. The colored circles (magenta, yellow, green, cyan) refer to pure species lifetime locations of the epithelial FLIM-probes respectively. The lines connecting the colored circles indicate the expected trajectory of pixels containing a range of linear combinations of fractional lifetime of each of the two pure species. The results indicate experimental pixel lifetimes of dual-probe stained images fall linearly between the two pure probe locations for most combinations of 2 probes. Certain conditions where mismatches occurred in brightness of fluorescent species resulted in one fluorescent species dominating, resulting in fractional lifetimes being more heavily weighted to one end of the trajectory line.

These phasors were piped into the trained model which resulted in an array of values ranging from 0 to 1 for the probabilities codifying likelihood of the number and specific identities of FLIM-probes present amongst all possible experimental conditions, see select examples in **Fig. 2.15**. Next, previous single-probe stained images were used to compute 2D histograms of collected pixel lifetime coordinates across two harmonics. The coordinate bins with maximum counts were used to identify the single pure component coordinates in each harmonic and used as a basis for constructing the linear system of equations. The model results informed the phasor analysis by reducing the system from four to two

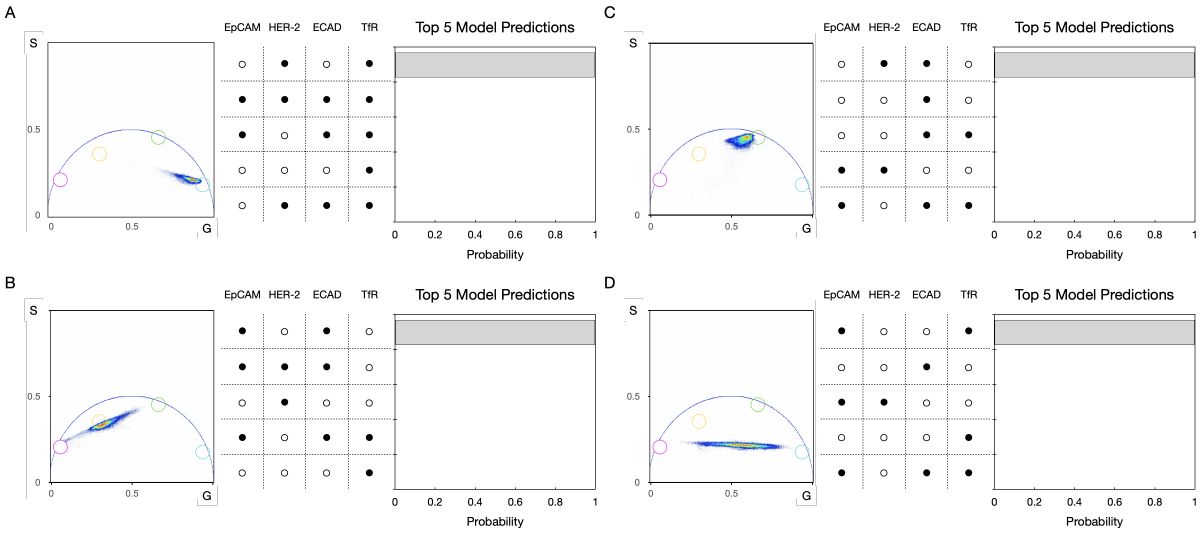

Figure 2.15: Top 5 Model Prediction Probabilities for Select Dual-probe Examples. Phasor distributions and corresponding top 5 model predicted probabilities. Model prediction (gray bars) correctly identify number and type of contributing fluorescent probe-marker pairs.

dimensions, or unknown lifetime fractions, simplifying computation of non-zero fractional lifetime for only the two probes that matched staining conditions. The linearity also suggests absence of interaction or energy transfer between the probes despite targeting co-localized regions.

Original total intensity and reconstructed images for all 4 possible channels were normalized and pseudo-colored to match the colored circles on the phasor, shown in **Fig. 2.16(i,iii-vi)**. The results indicate positive signal in the appropriate stained channels and elimination of the punctate, sparse false positive signal in the unstained channels otherwise previously noted. Specificity of staining was maintained, matching expectations had different samples been stained individually for each of the two probes employed or with two spectrally different colored probes. This demonstrates unbiased dimensional reduction via deep learning not only reduced "signal bleed-through" but also results in improved signal-to-noise and automation of analysis.

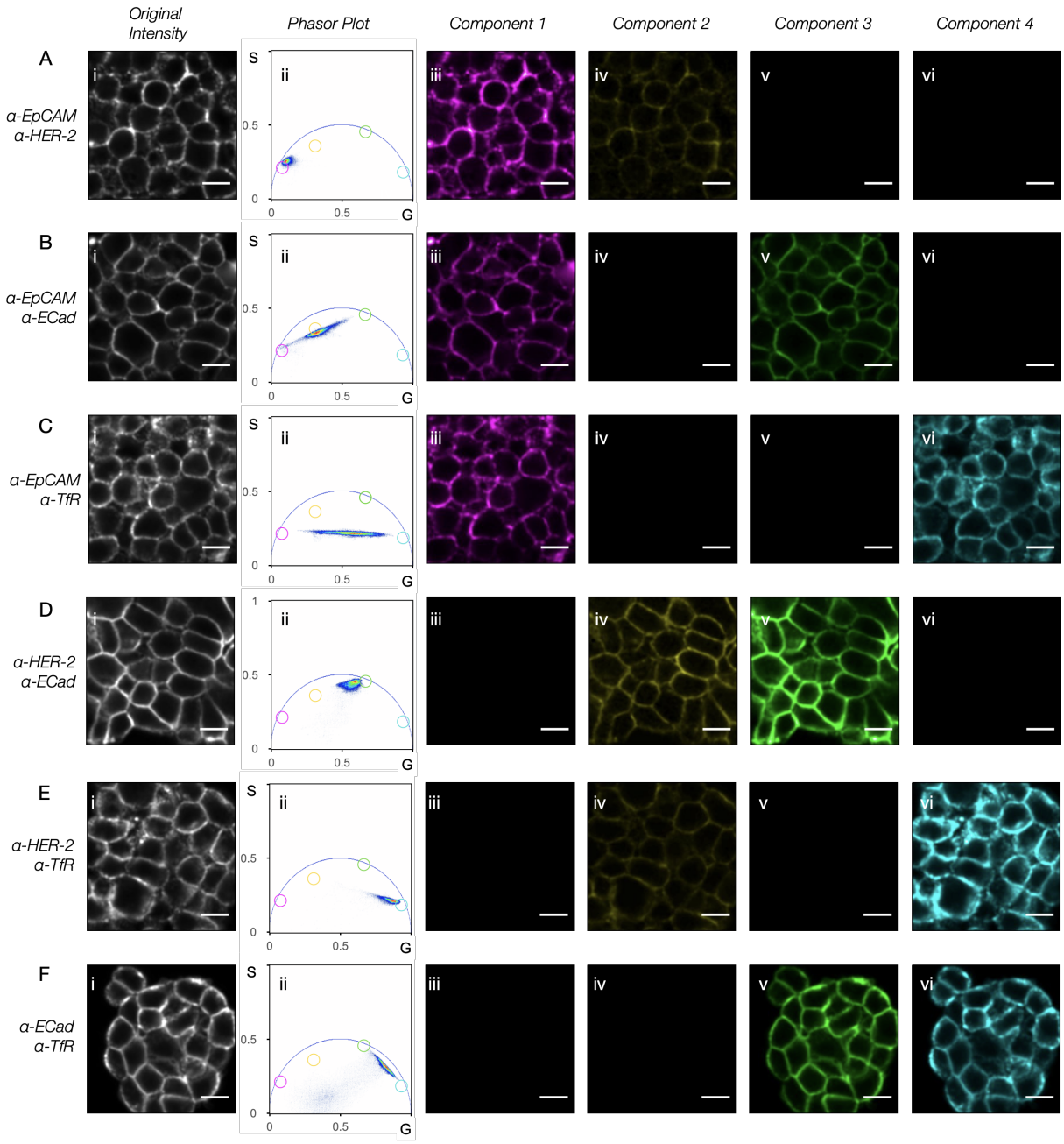

Figure 2.16: Resolved Dual-probe Images via Dimensional Reduction and Deep Learning. (A-F) Bt474 cells stained with combinations of 2 FLIM-probes targeting EpCAM, HER-2, ECad, and TfR respectively.(i) original total intensity images, (ii) corresponding first harmonic phasor plots, laser frequency=20MHz, and (iii-vi) resolved and reconstructed component-specific fluorescence images after phasor analysis. Scale bars=20μm.

2.6.2 Resolution of Triple-Probe Stained Samples

Extending this approach, we implemented the deep learning classifier on all 4 sample combinations stained with 3 FLIM-probes (triple-probe stains) to demonstrate the robustness of false positive signal reduction when resolving multiplexed molecular probes within the same spectral window. Here, experiments are analogous to traditional three-color immunofluorescence microscopy. In each experiment, Bt474 cells were stained consecutively with 3 of the 4 possible FLIM-probes prior to imaging. Experiments were arranged to comprise all four possible combinations of 3-probe staining conditions given the four previously conjugated probes (EpCAM-QD585, HER2-KU530, ECAD-Bodipy-TMR, and Tfr-AF555). The intensity and lifetime signals were recorded, transformed, median filtered, and plotted on the phasor. Each panel in **Fig. 2.17** shows the phasors corresponding to each staining condition. Once again, the colored circles (magenta, yellow, green, cyan) refer to pure species lifetime locations of the epithelial FLIM-probes respectively. Here, the triangles connecting the colored circles indicate the expected locations of pixels depending on the linear combination of fractional lifetime from each of the three pure species located on the vertices. The results indicate majority of experimental pixel lifetimes of triple-probe stained images fall within the demarcated region defined by the three pure probe locations for all combinations of 3 probes. Similarly to dual-probe analysis, the model evaluated phasors, producing an array of probabilities for the likelihood of the number and specific identities of FLIM-probes present amongst all possible multi-probe experimental conditions, see select examples in **Fig. 2.18**. The unknown fractions of the linear system were reduced to only the most likely probes identified, and non-zero lifetime fractions for only these 3 identified probes were resolved. Images in **Fig. 2.17(iii-vi)** were normalized and pseudo-colored to match the colored circles on the phasor and show original total intensity followed by the reconstructed images for each probes channel. The results once again match expectations had different samples

been stained individually for each of the three probes employed or three spectrally different colored probes been used. This further indicated reproducibility of the staining specificity and sample histology after resolving three spectrally overlapping molecular probes using deep learning and the phasor approach to FLIM. Here we have extended the capability to multiplex spatially co-localized exogenous molecular probes within the same spectral channel while reducing signal bleed through when using non ideal fluorescent species.

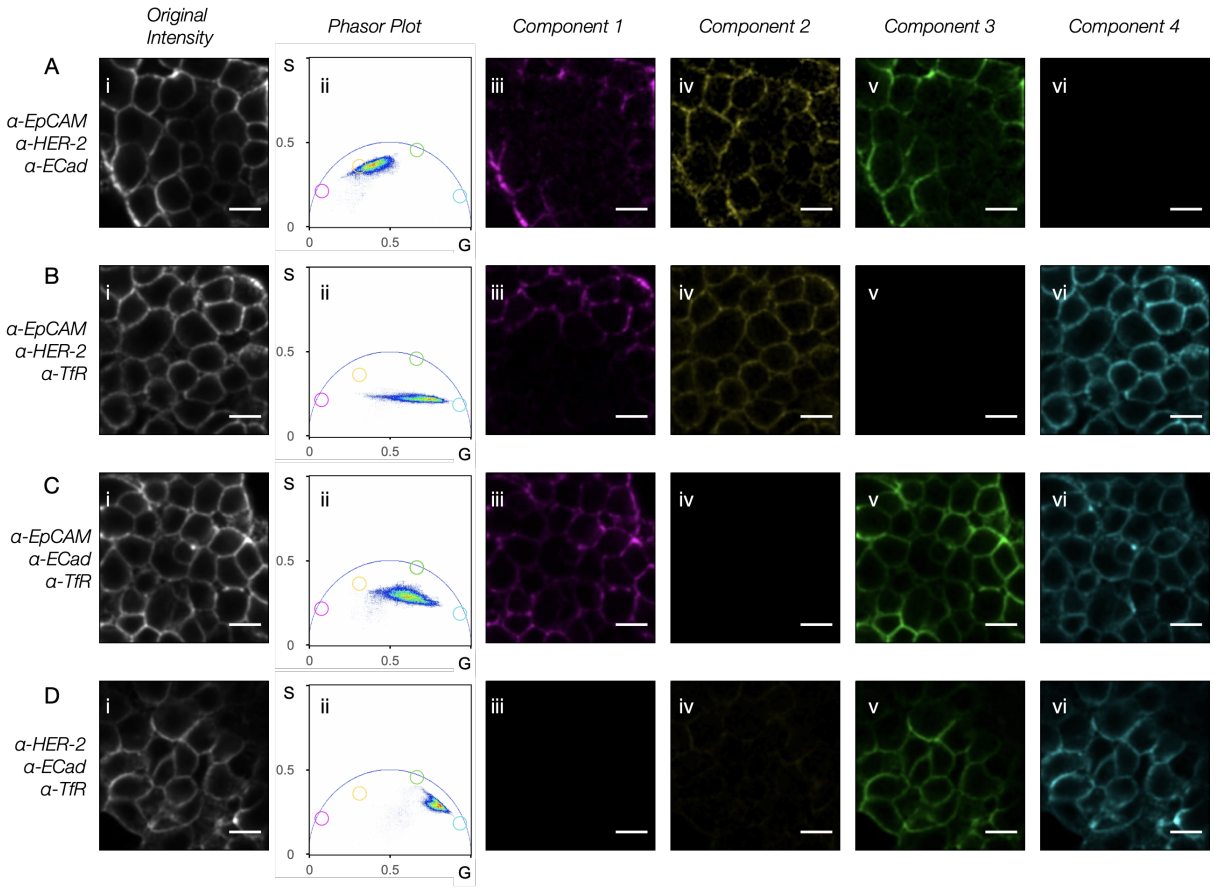

Figure 2.17: Resolved Triple-probe Images via Dimensional Reduction and Deep Learning. (A-D) Bt474 cells stained with combinations of 3 FLIM-probes targeting EpCAM, HER-2, ECad, and TfR respectively.(i) original total intensity images, (ii) corresponding first harmonic phasor plots, laser frequency=20MHz, and (iii-vi) resolved and reconstructed component-specific fluorescence images after phasor analysis. Scale bars=20μm.

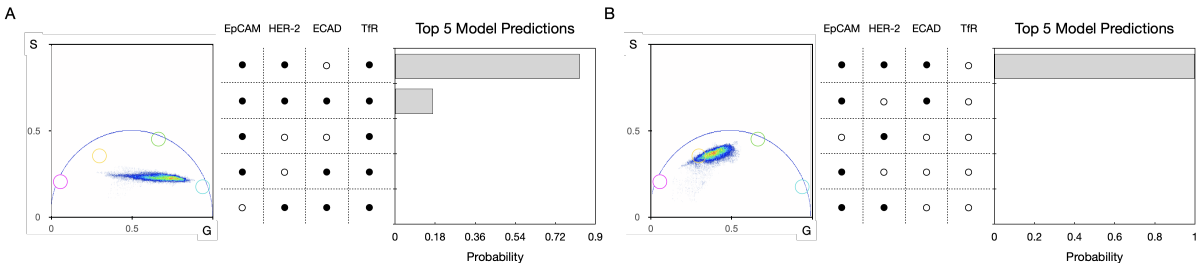

Figure 2.18: Top 5 Model Prediction Probabilities for Select Triple-probe Examples. Phasor distributions and corresponding top 5 model predicted probabilities. Model prediction (gray bars) correctly identify number and type of contributing fluorescent probe-marker triplets.

2.6.3 Resolution of Quadruple-Probe Stained Cell Line Samples

To further demonstrate the FLIM-based molecular profiling platform, we multiplexed all 4 FLIM-probes (quadruple-probe stains) to extend capabilities of multiplexing not only within the same spectral window but across cellular phenotypes using lifetime information alone. In addition to Bt474 cells, human breast cancer cell lines MCF-7 and SKBR3 were stained consecutively with all 4 possible FLIM-probes (EpCAM-QD585, HER2-KU530, ECAD-Bodipy-TMR, and Tfr-AF555). Cell lines were chosen to demonstrate evaluation of samples with variable expression patterns. MCF-7 in particular exhibits very low expression of HER-2 complementing the high expression of the other two cell lines. HER-2 expression traditionally guides clinical management of breast cancer and indicates therapeutic choice. As a result, it serves as a model for demonstrating the practical role and future clinical utility of multiplexed molecular profiling platforms like the one described here. The intensity and lifetime signals for Bt474, SKBR3, and MCF-7 were recorded, transformed, median filtered, and plotted on the phasors in **Fig. 2.19** respectively. Colored circles again refer to the four pure component lifetime locations and demarcate the vertices of the quadrilateral that defines the region in which pixels are expected to fall. Results confirm that majority of experimental pixel lifetimes fall within this region which confirms continued applicability of the law of linear combination. Probe-specific intensity

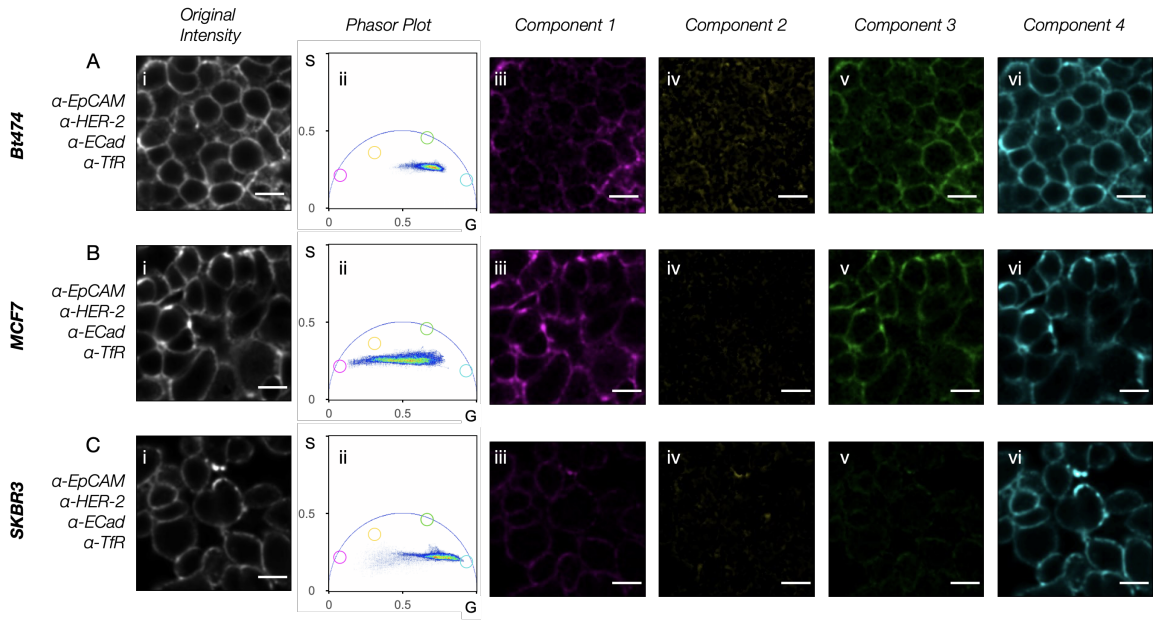

Figure 2.19: Resolved Quadruple-probe Images via Dimensional Reduction and Deep Learning. (A-C) Bt474, MCF7, SKBR3 cells stained with all 4 FLIM-probes targeting EpCAM, HER-2, ECad, and TfR respectively.(i) original total intensity images, (ii) corresponding first harmonic phasor plots, laser frequency=20MHz, and (iii-vi) resolved and reconstructed component-specific fluorescence images after phasor analysis. Scale bars=20μm.

images were reconstructed as before and resulting pseudo-colored images are shown in **Fig. 2.19(iii-vi)**. The results once again match expectations of multi-color immunofluorescence microscopy and preservation of staining specificity and sample histology after resolving all 4 spectrally overlapping molecular probes using the phasor approach to FLIM.

Here each sample type exhibits expressional activity for each of the four target markers. As a result, dimensional reduction is not necessary when multiplexing all 4 probes simultaneously. However, in the event samples are truly negative for one or more target marker, dimensional reduction becomes salient and a deep learning approach enables resolution agnostic to sample identity and irrespective of a-priori knowledge of probes used. Moreover, it becomes imaginable that sample marker expression, albeit not entirely absent, is low enough below thresholded value and as such for clinical utility can be categorized the same as a negative expression. HER-2 expression is a reasonable approximation as it's utility in clinical management of breast cancer is more binary in nature. As a result, MCF7

cells, known to be low HER-2 expressors can stand to benefit from dimensional reduction from a quadruple-stained sample to a triple-stained sample resulting in both clear demarcation of below threshold HER-2 expression and improved signal-to-noise for the remaining three molecular markers.

Additional set of split violin plots, **Fig. 2.20** of reconstructed intensity images compare intensity distributions of all 1-, 2-, 3-, and 4-probe Bt474 experiments with and without implementation of machine learning. Across all 1-, 2-, and 3-probe conditions specifically, the data clearly indicates reduction of "signal bleed through" as seen by reduction of positive distributions in untagged channels. This elimination of false positives (red asterisks) improves accuracy of resolution. The effect is the result of the deep learning classifier restricting distribution of signal intensity solely to the specific and correct component channels. Additionally, a greater fraction of signal was recovered in the KU-dependent channel. This resulted from prevention of KU-specific signal being incorrectly attributed as a combination of signal from the other probes. Without implementation of machine learning, pixels that fall near the 3 linear segments between Quantum Dot 585, KU530, and Bodily TMR probes resulted in noisier pixels within a distribution being falsely attributed as a linear combination of the others due to their proximity. Conversely, false positives were not significantly present in the AF555-dependent channel and intensity distributions did not vary with the addition of machine learning as noted by the symmetry of the violin plots in **Fig. 2.20D**. The juxtaposition of these two opposing effects further highlights the practical advantages realized by implementation of the deep learning classification model and also underscore the importance of selection of fluorescent species linearly orthogonal in the phasor domain. Future development of additional spectrally matched long-lifetime probes or engineering probes with tunable intrinsic lifetimes will strongly complement the multiplexed platform.

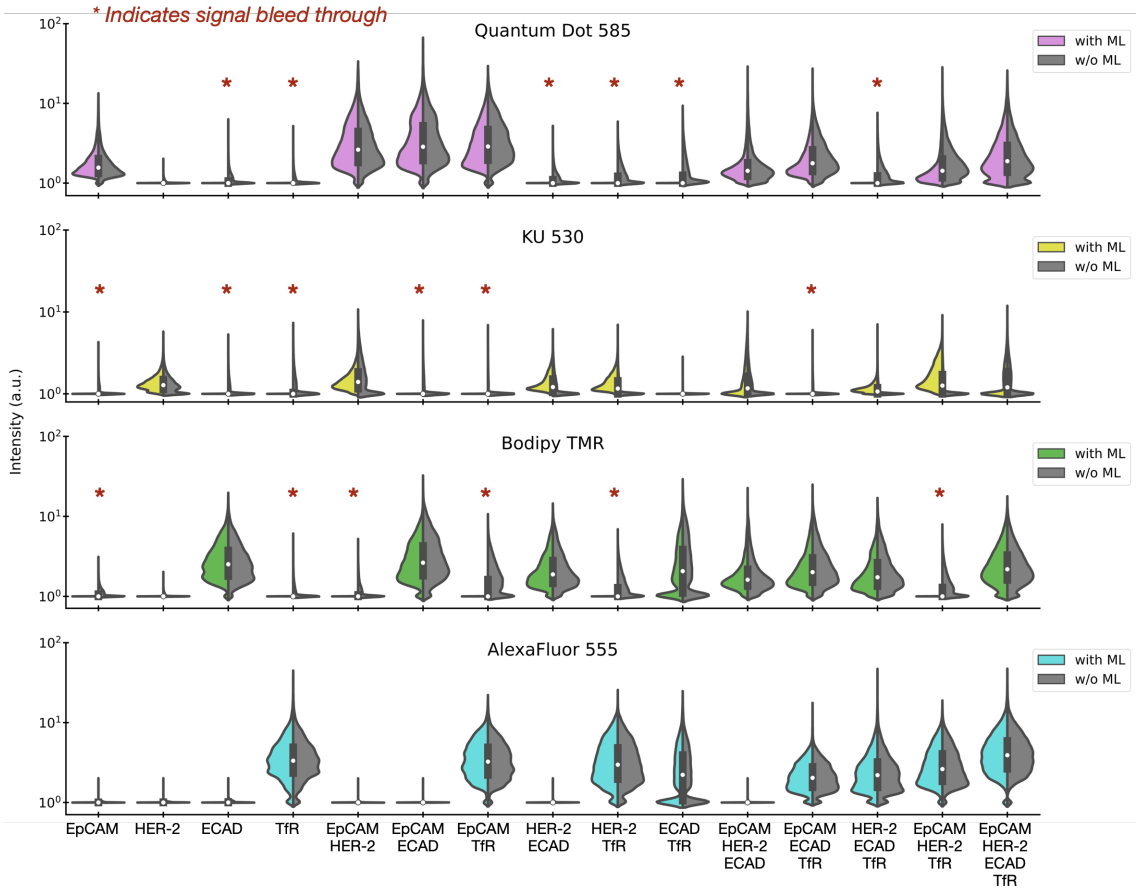

Figure 2.20: Intensity Distributions Across All 4-probe Multiplexed Studies. Violin plots of individual resolved images from various experimental probe staining conditions after implementation of machine learning dimensional reduction according to EpCAM, HER-2, ECad, and Tfr channels respectively.

Resolution of single-probe stained images confirmed maintenance of analysis accuracy despite introduction of an upstream deep learning module. Additionally, resolved single-probe experiments are the direct benchmark against standard spectral imaging and are necessary for quantitative comparison of multiplexed results. Mean intensities for each marker-specific reconstructed image in quadruple-probe experiments were averaged across 6 replicates and 3 different cell lines, **Fig. 2.21**.

White bars plot original mean intensity of images from single-probe stained experiments as a benchmark for comparison. Gray bars correspond to images resolved from quadruple-probe stained experiments. Mean intensities of 4-probe multiplexed, lifetime

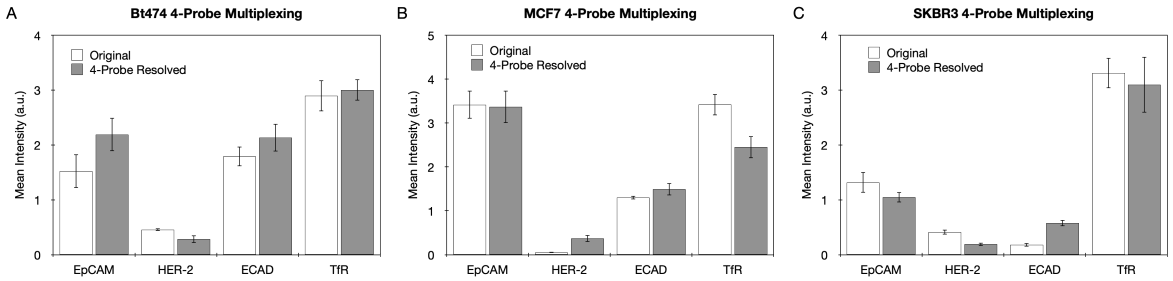

Figure 2.21: Mean Intensity of Resolved Probe-specific Multiplexed Channels Compared to Original. Mean intensity of all 4 resolved probes (gray) and 4 single stained images using standard spectral imaging (white). (A-C) in Bt474, MCF7, SKBR3 cell samples respectively. Means calculated as Grand Mean of mean image intensity across 6 replicate conditions.

resolved images relatively approximate original image intensities within standard error when coarsely categorizing signal into HIGH, MED, LOW. For certain applications this may be sufficient, however for finer quantification of expressional status a few identifiable contributors remain. First, quality of probes with respect to linear orthogonality, intensity-matching, and degree of lifetime variance present in cellular environments are main contributors. These impact how representative a single lifetime coordinate for pure components are relative to the distribution of lifetimes across all pixels. As a result this directly affects the analytical solution of fractional lifetime. As identified, the mediocre phasor location and dimness of the KU530 probe specifically is largest to blame. However, the specific fluorescent species used here are largely irrespective of underlying analytical methods of the multiplexed molecular imaging platform described, which remain fundamental and generalizable to advancing multiplexed lifetime imaging. Due to the modular nature of FLIM-probes, alternative fluorescent species with better intrinsic characteristics (lifetime, complexity) can be used. Additional work in the development of distinct and stable fluorescent species for use as molecular FLIM-probes is both ongoing and needed to realize the full potential of the lifetime multiplexing strategy described here. Secondly, averaging intensity across entire image replicates is an indirect measure of cellular and sub-cellular heterogeneity of expression. Moreover, image to image variations

in size, total cell count, and resulting fraction of intracellular or inter-cellular background likely contribute to mismatches in quantification by skewing descriptive statistics. Instead both pixel-level and per-cell analyses will better capture variability present within a sample. Due to the reciprocity of the phasor approach to FLIM, and the resulting mapping of fluorescent species identity to location in an image can be used to investigate sub-cellular spatial distributions of markers or time-linked changes in molecular feature integrity[61]. Additionally, per-cell statistics of signal intensity rely on segmentation of individual cells in images. Although achievable, manual approaches are tedious, inconsistent, and untenable in scalability. Alternatively, unsupervised clustering and deep learning techniques automate object-level image segmentation[61]. Although not demonstrated here, such techniques address current limitations in resolution of quantification of 4-probe multiplexed systems.

2.6.4 Pixel-Level Resolution

Lastly, pixel-level analysis characterized number and distribution of probe species, validating sub-cellular tracking with expected staining specificity. Since targeted markers are all expressed at the cell membrane surface, distribution of pixels containing multiple probes were predicted to spatially align with the cellular membrane. Indices of each reconstructed intensity image were aligned and masked for positive signal. Mask cutoffs were defined by mean photon counts of greater than or equal to one. Binarizing results for each pixel across all probes employed resulted in probe number quantification for each of the three cell types. The heat maps in **Fig. 2.22B** paint pixels by color dependent on number of probes present. Regions with the highest intensity, corresponding to number of probes present, spatially tracked with the surface of the cell membrane. Moreover, the bar charts in **Fig. 2.22A** depict the percentage of pixels containing a particular number of probes. While both Bt474 and SKBR3 images contain a percentage of pixels containing 4 probes, less than 0.1% of MCF-7 image pixels do. The data suggests majority of MCF-7

image pixels have at most 3 or fewer probes with the most found in regions at the cell membrane surface. This was expected since MCF-7 cells exhibit lower expression of HER-2. As an example, this might be clinically useful in determining that treatment with Herceptin is not indicated here. Moreover, the data suggests this approach is capable of resolving up to four spectrally overlapping molecular probes spatially targeting the same cellular compartment at the pixel-level. Furthermore, pixels here span a distance of 0.41μm indicating FLIM-based multiplexing of molecular probes are conceivably resolvable within a 2-dimensional sub-cellular footprint of the cell membrane surface, 0.17μm^2 in area. Another benefit over colored probes is minimal likelihood that analysis is subject to spectral crosstalk within such close proximity since probes are spectrally overlapping.

In summary, these results demonstrate 4-probe multiplexing of spatially co-localized surface targets with exogenous molecular probes within the same spectral channel. This

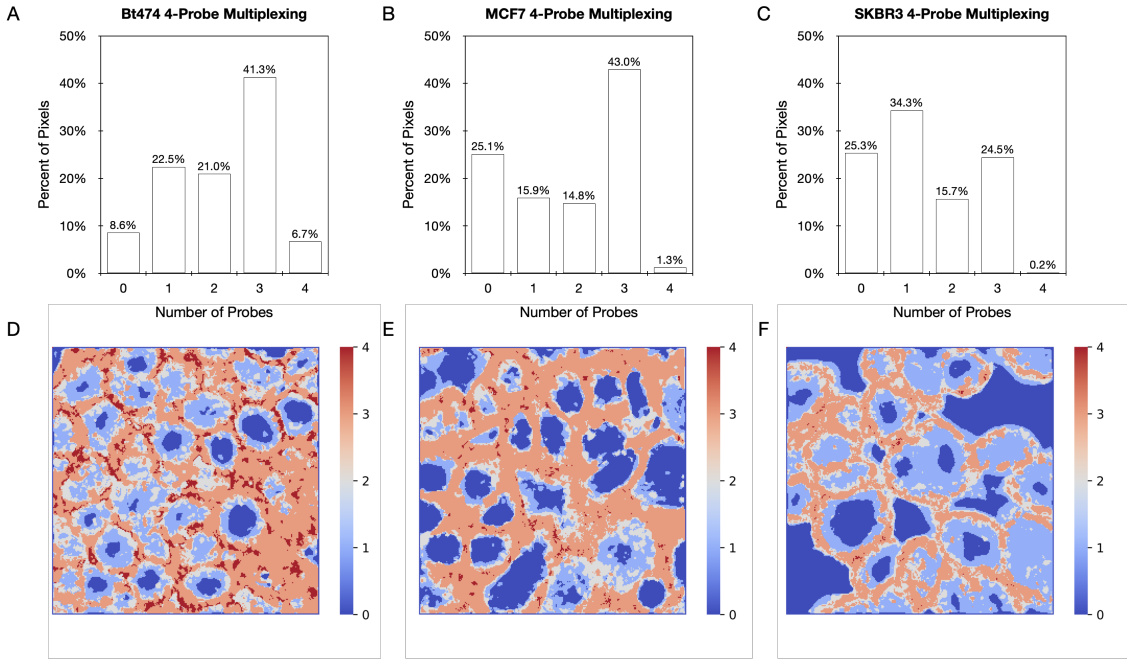

Figure 2.22: Pixel-level Spatial Resolution and Heatmapping. (A-C) Bar chart plotting percentage of total pixels containing labeled number of different fluorescent species across Bt474, MCF7, and SKBR3 cell samples respectively. (D-F) Heatmap generated by color mapping pixels with differing number of fluorescent components ranging from 4 (red) to 0 (blue).

work qualitatively unmixes probe-specific signal and although limited, achieves coarse quantification, establishing the a foundation and roadmap to improved resolution of molecular expression using lifetime information alone.

2.7 Conclusion

Multiplexed molecular profiling that preserves spatial context traditionally requires either spectral differentiation, high-powered imaging equipment, or cyclic techniques involving serially degradative rounds of sample staining and antigen retrieval. The phasor approach to fluorescence lifetime imaging microscopy (FLIM) is a fit-free method for facile analysis of fluorescence lifetime by transforming and mapping complex exponential decay curves onto a powerful and informative geometric-graphical representation. As a result of the transformation, resolving mixtures of fluorescent species and their corresponding multi-exponential decays becomes a simplified linear system of equations. Moreover, pattern-recognition via machine learning provides avenues to further exploit the graphical visualization of lifetime data. Here we demonstrate a multiplexed platform leveraging the phasor approach to FLIM for simple, rapid resolution of up to 4 exogenous molecular probes within a single spectral window, adding an orthogonal dimension with which to multiplex.

We employed up to four tumor-specific FLIM-probes targeting spatially co-localized cell surface biomarkers simultaneously within a single sample. Using lifetime information alone, total sample signal intensity was resolved into probe-specific contributions, making it analogous to imaging four separate spectrally distinct probes. Additionally, implementation of deep learning classification of phasor data enables both dimensional reduction for improved resolution and a clinically tenable path towards scalability and platform automation.

Improving our understanding of the molecular heterogeneity within the tumor microenvironment can help characterize host vs. neoplastic cell types, identify morphological changes indicative of prognosis, guide clinical management through molecular sub-typing, or elucidate novel targets further complementing drug discovery efforts. In order to best capture this rich and informative landscape, improvements in multiplexing capacity of molecular profiling platforms are necessary. Advantageously, multiplexing within a single spectral window preserves remaining spectral range for additional increases in multiplexing. Circumventing concerns of spectral overlap that limit simultaneous use of colored probes to a handful of spectral windows, the approach here is capable of achieving 4 lifetime probes across each spectral window for at least a 4x multiplicative increase in multiplexing capacity.

Current state-of-the-art hyper-spectral imaging techniques have furthered mapping the molecular geography of pathological tissue. The advances demonstrated here in multiplexing, realized by the addition of fluorescence lifetime imaging and molecular feature classification through machine learning, complement these techniques. Overall, the data illustrates the ability of the deep learning classification model to dimensionally reduce and analytically resolve 4-component systems blind to specific cell type. These results are particularly powerful in the context of future FLIM-based applications involving profiling heterogeneous cell samples, such as FFPE tissue and clinical biopsies, to provide actionable information through multiplexed quantification of molecular expression.

2.8 Future Perspectives: A Foward Look

2.8.1 Additional Lifetime Probes and Multiplexing Capacity

The combination of Phasor FLIM analysis and deep learning has enabled resolution of up to 4 spatially coexistent cellular targets at the individual pixel level using lifetime information alone. Challenges resulting from the limited availability of spectrally-matched long-lifetime fluorescent probes further highlight the growing need for the development of additional lifetime probes. In the future, manipulating fluorescent species through controlled quenching or dynamic biophysical molecular interactions will afford probes with tunable lifetimes. The addition of lifetime probes combined with instrumentation for the collection of higher harmonics wold allow further multiplexing within a given spectral window. Additionally, extending lifetime multiplexing across remaining spectral windows would enable multiplicative increases in total multiplexing capacity, outpacing standard spectral imaging.

2.8.2 Applications of Machine Learning in Phasor FLIM

Further improvements in automation and analysis could be realized by implementing additional machine learning methods. Beyond image segmentation, clustering methods such as Gaussian Mixture Models (GMM) and Density Based Spatial Clustering of Applications with Noise (DBSCAN) will likely leverage both the geometric-graphical and reciprocal aspects of Phasor FLIM for more robust and translatable features.

Bibliography

[1] Lorenz M Mayr and Peter Fuerst. The Future of High-Throughput Screening. 2008.

[2] Saurabh Vyawahare, Andrew D. Griffiths, and Christoph A. Merten. Miniaturization and Parallelization of Biological and Chemical Assays in Microfluidic Devices. *Chemistry & Biology*, 17(10):1052–1065, oct 2010.

[3] Luoran Shang, Yao Cheng, and Yuanjin Zhao. Emerging Droplet Microfluidics, jun 2017.

[4] Mira T. Guo, Assaf Rotem, John A. Heyman, and David A. Weitz. Droplet microfluidics for high-throughput biological assays, jun 2012.

[5] Pingan Zhu and Liqiu Wang. Passive and active droplet generation with microfluidics: a review. *Lab on a Chip*, 17(1):34–75, jan 2017.

[6] Shia Yen Teh, Robert Lin, Lung Hsin Hung, and Abraham P. Lee. Droplet microfluidics, jan 2008.

[7] Emory M. Payne, Daniel A. Holland-Moritz, Shuwen Sun, and Robert T. Kennedy. High-throughput screening by droplet microfluidics: Perspective into key challenges and future prospects. *Lab on a Chip*, 20(13):2247–2262, 2020.

[8] María Díaz-González, César Fernández-Sánchez, and Antonio Baldi. Multiple actuation microvalves in wax microfluidics. *Lab Chip*, c(20):3969–3976, oct 2016.

[9] Robin H. Liu, Justin Bonanno, Jianing Yang, Ralf Lenigk, and Piotr Grodzinski. Single-use, thermally actuated paraffin valves for microfluidic applications. *Sensors and Actuators, B: Chemical*, 98(2-3):328–336, mar 2004.

[10] Elizabeth A. Phillips, Rui Shen, Siyu Zhao, and Jacqueline C. Linnes. Thermally actuated wax valves for paper-fluidic diagnostics. *Lab on a Chip*, 16(21):4230–4236, oct 2016.

[11] M. Díaz-González, G. Boix, C. Fernández-Sánchez, and A. Baldi. Wax microfluidics light-addressable valve with multiple actuation. *Smart Sensors, Actuators, and MEMS VIII*, 10246(May 2017):102460G, 2017.

[12] Jin Yuan Qian, Cong Wei Hou, Xiao Juan Li, and Zhi Jiang Jin. *Actuation mechanism of microvalves: A review*, volume 11. 2020.

[13] Chong H Oh, Kwang W, Ahn. A review of microvalves. *JOURNAL OF MICROMECHANICS AND MICROENGINEERING*, 2006.

[14] Hakim Boukellal, Seila Selimović, Yanwei Jia, Galder Cristobal, and Seth Fraden. Simple, robust storage of drops and fluids in a microfluidic device. *Lab Chip*, 9(2):331–8, 2009.

[15] Rebecca R Pompano, Weishan Liu, Wenbin Du, and Rustem F Ismagilov. Microfluidics Using Spatially Defined Arrays of Droplets in One, Two, and Three Dimensions. *The Annual Review of Analytical Chemistry is online Annual Rev. Anal. Chem*, 4:59–81, 2011.

[16] Meng Sun, Swastika S Bithi, and Siva A Vanapalli. Microfluidic static droplet arrays with tuneable gradients in material composition. *Lab on a Chip*, 11(23):3949–3952, 2012.

[17] Akkapol Suea-Ngam, Philip D. Howes, Monpichar Srisa-Art, and Andrew J. Demello. Droplet microfluidics: From proof-of-concept to real-world utility? *Chemical Communications*, 55(67):9895–9903, 2019.

[18] Ismail Emre Araci and Philip Brisk. Recent developments in microfluidic large scale integration. *Current Opinion in Biotechnology*, 25:60–68, 2014.

[19] Kassa Semagn, • Raman Babu, Sarah Hearne, and Michael Olsen. Single nucleotide polymorphism genotyping using Kompetitive Allele Specific PCR (KASP): overview of the technology and its application in crop improvement.

[20] Douglas Hanahan and Robert A. Weinberg. Hallmarks of cancer: The next generation, mar 2011.

[21] Rebecca A. Burrell, Nicholas McGranahan, Jiri Bartek, and Charles Swanton. The causes and consequences of genetic heterogeneity in cancer evolution, sep 2013.

[22] Corbin E. Meacham and Sean J. Morrison. Tumour heterogeneity and cancer cell plasticity, 2013.

[23] Samy Lamouille, Jian Xu, and Rik Derynck. Molecular mechanisms of epithelial-mesenchymal transition, mar 2014.

[24] Tuan Zea Tan, Qing Hao Miow, Yoshio Miki, Tetsuo Noda, Seiichi Mori, Ruby Yun[U+2010]Ju Huang, and Jean Paul Thiery. Epithelial[U+2010]mesenchymal transition spectrum quantification and its efficacy in deciphering survival and drug responses of cancer patients. *EMBO Molecular Medicine*, 6(10):1279–1293, oct 2014.

[25] Ian Y. Wong, Sarah Javaid, Elisabeth A. Wong, Sinem Perk, Daniel A. Haber, Mehmet Toner, and Daniel Irimia. Collective and individual migration following the epithelial-mesenchymal transition. *Nature materials*, 13(11):1063–1071, nov 2014.

[26] Paul F. Lindholm, Yi Lu, Brian P. Adley, Tudor Vladislav, Borko Jovanovic, Neela Sivapurapu, Ximing J. Yang, and André Kajdacsy-Balla. Role of monocyte-lineage cells in prostate cancer cell invasion and tissue factor expression. *The Prostate*, 70(15):1672–1682, nov 2010.

[27] David S Hsu, Mickey K Kim, Bala S. Balakumaran, Chaitanya R Acharya, Carey K Anders, Tim Clay, H. Kim Lyerly, Charles G. Drake, Michael A. Morse, and Phillip G. Febbo. Immune Signatures Predict Prognosis in Localized Cancer. *Cancer Investigation*, 28(7):765–773, jul 2010.

[28] Karen S. Sfanos, Tullia C. Bruno, Alan K. Meeker, Angelo M. De Marzo, William B. Isaacs, and Charles G. Drake. Human prostate-infiltrating CD8+ T lymphocytes are oligoclonal and PD-1+. *Prostate*, 69(15):1694–1703, nov 2009.

[29] Joseph C. Klink, Lionel L. Bañez, Leah Gerber, Amy Lark, Robin T. Vollmer, and Stephen J. Freedland. Intratumoral inflammation is associated with more aggressive prostate cancer. *World Journal of Urology*, 31(6):1497–1503, dec 2013.

[30] G. Comito, E. Giannoni, C. P. Segura, P. Barcellos-De-Souza, M. R. Raspollini, G. Baroni, M. Lanciotti, S. Serni, and P. Chiarugi. Cancer-associated fibroblasts and M2-polarized macrophages synergize during prostate carcinoma progression. *Oncogene*, 33(19):2423–2431, may 2014.

[31] Jérôme Galon, Helen K. Angell, Davide Bedognetti, and Francesco M. Marincola. The Continuum of Cancer Immunosurveillance: Prognostic, Predictive, and Mechanistic Signatures, jul 2013.

[32] Maria Gabriela Anitei, Guy Zeitoun, Bernhard Mlecnik, Florence Marliot, Nacilla Haicheur, Ana Maria Todosi, Amos Kirilovsky, Christine Lagorce, Gabriela Bindea, Dan Ferariu, Mihai Danciu, Patrick Bruneval, Viorel Scripcariu, Jean Marc Chevallier, Franck Zinzindohoué, Anne Berger, Jérôme Galon, and Franck Pagès. Prognostic and predictive values of the immunoscore in patients with rectal cancer. *Clinical Cancer Research*, 20(7):1891–1899, apr 2014.

[33] Jérôme Galon, Franck Pagès, Francesco M. Marincola, Helen K. Angell, Magdalena Thurin, Alessandro Lugli, Inti Zlobec, Anne Berger, Carlo Bifulco, Gerardo Botti, Fabiana Tatangelo, Cedrik M. Britten, Sebastian Kreiter, Lotfi Chouchane, Paolo Delrio, Hartmann Arndt, Martin Asslaber, Michele Maio, Giuseppe V. Masucci, Martin Mihm, Fernando Vidal-Vanaclocha, James P. Allison, Sacha Gnjatic, Leif Hakansson, Christoph Huber, Harpreet Singh-Jasuja, Christian Ottensmeier, Heinz Zwierzina, Luigi Laghi, Fabio Grizzi, Pamela S. Ohashi, Patricia A. Shaw, Blaise A. Clarke, Bradly G. Wouters, Yutaka Kawakami, Shoichi Hazama, Kiyotaka Okuno, Ena Wang, Jill O'Donnell-Tormey, Christine Lagorce, Graham Pawelec, Michael I. Nishimura, Robert Hawkins, Réjean Lapointe, Andreas Lundqvist, Samir N. Khleif, Shuji Ogino, Peter Gibbs, Paul Waring, Noriyuki Sato, Toshihiko Torigoe, Kyogo Itoh, Prabhu S. Patel, Shilin N. Shukla, Richard Palmqvist, Iris D. Nagtegaal, Yili Wang, Corrado D'Arrigo, Scott Kopetz, Frank A. Sinicrope, Giorgio Trinchieri, Thomas F. Gajewski, Paolo A. Ascierto, and Bernard A. Fox. Cancer classification using the Immunoscore: A worldwide task force, oct 2012.

[34] Jérôme Galon, Bernhard Mlecnik, Gabriela Bindea, Helen K Angell, Anne Berger, Christine Lagorce, Alessandro Lugli, Inti Zlobec, Arndt Hartmann, Carlo Bifulco, Iris D

Nagtegaal, Richard Palmqvist, Giuseppe V Masucci, Gerardo Botti, Fabiana Tatangelo, Paolo Delrio, Michele Maio, Luigi Laghi, Fabio Grizzi, Martin Asslaber, Corrado D'Arrigo, Fernando Vidal[U+2010]Vanaclocha, Eva Zavadova, Lotfi Chouchane, Pamela S Ohashi, Sara Hafezi[U+2010]Bakhtiari, Bradly G Wouters, Michael Roehrl, Linh Nguyen, Yutaka Kawakami, Shoichi Hazama, Kiyotaka Okuno, Shuji Ogino, Peter Gibbs, Paul Waring, Noriyuki Sato, Toshihiko Torigoe, Kyogo Itoh, Prabhu S Patel, Shilin N Shukla, Yili Wang, Scott Kopetz, Frank A Sinicrope, Viorel Scripcariu, Paolo A Ascierto, Francesco M Marincola, Bernard A Fox, and Franck Pagès. Towards the introduction of the 'Immunoscore' in the classification of malignant tumours. *The Journal of Pathology*, 232(2):199–209, jan 2014.

[35] Sathana Dushyanthen, Paul A. Beavis, Peter Savas, Zhi Ling Teo, Chenhao Zhou, Mariam Mansour, Phillip K. Darcy, and Sherene Loi. Relevance of tumor-infiltrating lymphocytes in breast cancer, aug 2015.

[36] R. Salgado, C. Denkert, S. Demaria, N. Sirtaine, F. Klauschen, G. Pruneri, S. Wienert, G. Van den Eynden, F. L. Baehner, F. Penault-Llorca, E. A. Perez, E. A. Thompson, W. F. Symmans, A. L. Richardson, J. Brock, C. Criscitiello, H. Bailey, M. Ignatiadis, G. Floris, J. Sparano, Z. Kos, T. Nielsen, D. L. Rimm, K. H. Allison, J. S. Reis-Filho, S. Loibl, C. Sotiriou, G. Viale, S. Badve, S. Adams, K. Willard-Gallo, and Sherene Loi. The evaluation of tumor-infiltrating lymphocytes (TILS) in breast cancer: Recommendations by an International TILS Working Group 2014, feb 2015.

[37] Sean J. Morrison and Allan C. Spradling. Stem Cells and Niches: Mechanisms That Promote Stem Cell Maintenance throughout Life, feb 2008.

[38] Andriy Marusyk, Doris P. Tabassum, Philipp M. Altrock, Vanessa Almendro, Franziska Michor, and Kornelia Polyak. Non-cell-autonomous driving of tumour growth supports sub-clonal heterogeneity. *Nature*, 514(7520):54–58, oct 2014.

[39] Joaquim Calbo, Erwin van Montfort, Natalie Proost, Ellen van Drunen, H. Berna Beverloo, Ralph Meuwissen, and Anton Berns. A Functional Role for Tumor Cell Heterogeneity in a Mouse Model of Small Cell Lung Cancer. *Cancer Cell*, 19(2):244–256, feb 2011.

[40] H. Raza Ali, Hartland W. Jackson, Vito R. T. Zanotelli, Esther Danenberg, Jana R. Fischer, Helen Bardwell, Elena Provenzano, Oscar M. Rueda, Suet-Feung Chin, Samuel Aparicio, Carlos Caldas, and Bernd Bodenmiller. Imaging mass cytometry and multiplatform genomics define the phenogenomic landscape of breast cancer. *Nature Cancer*, 1(2):163–175, feb 2020.

[41] Michael J. Gerdes, Christopher J. Sevinsky, Anup Sood, Sudeshna Adak, Musodiq O. Bello, Alexander Bordwell, Ali Can, Alex Corwin, Sean Dinn, Robert J. Filkins, Denise Hollman, Vidya Kamath, Sireesha Kaanumalle, Kevin Kenny, Melinda Larsen, Michael Lazare, Qing Li, Christina Lowes, Colin C. McCulloch, Elizabeth McDonough, Michael C. Montalto, Zhengyu Pang, Jens Rittscher, Alberto Santamaria-Pang, Brion D. Sarachan, Maximilian L. Seel, Antti Seppo, Kashan Shaikh, Yunxia

Sui, Jingyu Zhang, and Fiona Ginty. Highly multiplexed single-cell analysis of formalinfixed, paraffin-embedded cancer tissue. *Proceedings of the National Academy of Sciences of the United States of America*, 110(29):11982–11987, jul 2013.

[42] Takahiro Tsujikawa, Sushil Kumar, Rohan N Borkar, Joe W Gray, Paul W Flint, and Lisa M Coussens Correspondence. Quantitative Multiplex Immunohistochemistry Reveals Myeloid-Inflamed Tumor-Immune Complexity Associated with Poor Prognosis. *CellReports*, 19:203–217, 2017.

[43] Leeat Keren, Marc Bosse, Diana Marquez, Robert West, Sean C Bendall, and Michael Angelo. A Structured Tumor-Immune Microenvironment in Triple Negative Breast Cancer Revealed by Multiplexed Ion Beam Imaging In Brief. *Cell*, 174, 2018.

[44] Hartland W. Jackson, Jana R. Fischer, Vito R.T. Zanotelli, H. Raza Ali, Robert Mechera, Savas D. Soysal, Holger Moch, Simone Muenst, Zsuzsanna Varga, Walter P. Weber, and Bernd Bodenmiller. The single-cell pathology landscape of breast cancer. *Nature*, 578(7796):615–620, feb 2020.

[45] Ute Resch-Genger, Markus Grabolle, Sara Cavaliere-Jaricot, Roland Nitschke, and Thomas Nann. Quantum dots versus organic dyes as fluorescent labels. 2008.

[46] Bernd Bodenmiller. Multiplexed Epitope-Based Tissue Imaging for Discovery and Healthcare Applications, apr 2016.

[47] Pavel Zrazhevskiy, Shivang R. Dave, and Xiaohu Gao. Addressing key technical aspects of quantum dot probe preparation for bioassays. *Particle and Particle Systems Characterization*, 31(12):1291–1299, dec 2014.

[48] Hiromichi Tsurui, Hiroyuki Nishimura, Susumu Hattori, Sachiko Hirose, Ko Okumura, and Toshikazu Shirai. Seven-color fluorescence imaging of tissue samples based on fourier spectroscopy and singular value decomposition. *Journal of Histochemistry and Cytochemistry*, 48(5):653–662, 2000.

[49] Yury Goltsev, Nikolay Samusik, Julia Kennedy-Darling, Gustavo Vazquez, Sarah Black, and Garry P Nolan Correspondence. Deep Profiling of Mouse Splenic Architecture with CODEX Multiplexed Imaging In Brief A DNA barcoding-based imaging technique uses multiplexed tissue antigen staining to enable the characterization of cell types and dynamics in a model of autoimmune diseas. *Cell*, 174:968–981, 2018.

[50] Pavel Zrazhevskiy and Xiaohu Gao. Quantum dot imaging platform for single-cell molecular profiling. *Nature Communications*, 4(1):1–12, mar 2013.

[51] Pavel Zrazhevskiy, Lawrence D. True, and Xiaohu Gao. Multicolor multicycle molecular profiling with quantum dots for single-cell analysis. *Nature Protocols*, 8(10):1852–1869, oct 2013.

[52] Charlotte Giesen, Hao A.O. Wang, Denis Schapiro, Nevena Zivanovic, Andrea Jacobs, Bodo Hattendorf, Peter J. Schüffler, Daniel Grolimund, Joachim M. Buhmann, Simone Brandt, Zsuzsanna Varga, Peter J. Wild, Detlef Günther, and Bernd Bodenmiller. Highly multiplexed imaging of tumor tissues with subcellular resolution by mass cytometry. *Nature Methods*, 11(4):417–422, mar 2014.

[53] Ash A. Alizadeh, Victoria Aranda, Alberto Bardelli, Cedric Blanpain, Christoph Bock, Christine Borowski, Carlos Caldas, Andrea Califano, Michael Doherty, Markus Elsner, Manel Esteller, Rebecca Fitzgerald, Jan O. Korbel, Peter Lichter, Christopher E. Mason, Nicholas Navin, Dana Pe'Er, Kornelia Polyak, Charles W.M. Roberts, Lillian Siu, Alexandra Snyder, Hannah Stower, Charles Swanton, Roel G.W. Verhaak, Jean C. Zenklusen, Johannes Zuber, and Jessica Zucman-Rossi. Toward understanding and exploiting tumor heterogeneity, aug 2015.

[54] Dimitrios Zardavas, Alexandre Irrthum, Charles Swanton, and Martine Piccart. Clinical management of breast cancer heterogeneity, jul 2015.

[55] Ryan A. Colyer, Claudia Lee, and Enrico Gratton. A novel fluorescence lifetime imaging system that optimizes photon efficiency. *Microscopy Research and Technique*, 71(3):201–213, mar 2008.

[56] Markus Grabolle, Peter Kapusta, Thomas Nann, Xu Shu, Jan Ziegler, and Ute Resch-Genger. Fluorescence lifetime multiplexing with nanocrystals and organic labels. *Analytical Chemistry*, 81(18):7807–7813, sep 2009.

[57] Thomas Niehörster, Anna Löschberger, Ingo Gregor, Benedikt Krämer, Hans Jürgen Rahn, Matthias Patting, Felix Koberling, Jörg Enderlein, and Markus Sauer. Multi-target spectrally resolved fluorescence lifetime imaging microscopy. *Nature Methods*, 13(3):257–262, feb 2016.

[58] Michelle a Digman, Valeria R Caiolfa, Moreno Zamai, and Enrico Gratton. The phasor approach to fluorescence lifetime imaging analysis. *Biophysical journal*, 94(2):L14–6, 2008.

[59] Chiara Stringari, Amanda Cinquin, Olivier Cinquin, Michelle A Digman, Peter J Donovan, and Enrico Gratton. Phasor approach to fluorescence lifetime microscopy distinguishes different metabolic states of germ cells in a live tissue. *Nat Acad Sci Proc*, 108(33):13582–13587, 2011.

[60] Alexander Vallmitjana, Alexander Dvornikov, Belen Torrado, David M Jameson, Suman Ranjit, and Enrico Gratton. Methods and Applications in Fluorescence Resolution of 4 components in the same pixel in FLIM images using the phasor approach Resolution of 4 components in the same pixel in FLIM images using the phasor approach. *Methods Appl. Fluoresc*, 8:35001, 2020.

[61] Rupsa Datta, Tiffany M. Heaster, Joe T. Sharick, Amani A. Gillette, and Melissa C. Skala. Fluorescence lifetime imaging microscopy: fundamentals and advances in instrumentation, analysis, and applications. *Journal of Biomedical Optics*, 25(07):1, may 2020.